Characterizing Tropical Easterly Waves across Central America during the Organization of Tropical East Pacific Convection (OTREC) Experiment

YOLANDE L. SERRA,[a] BENJAMIN R. LINTNER,[b,c] ANA MARÍA DURÁN-QUESADA,[d,e] MARCIAL GARBANZO-SALAS,[d] DANIEL HERNÁNDEZ-DECKERS,[f] AND GIUSEPPE TORRI[g]

[a] *Cooperative Institute for Climate, Ocean, and Ecosystem Studies, University of Washington, Seattle, Washington*
[b] *Department of Environmental Sciences, Rutgers, The State University of New Jersey, New Brunswick, New Jersey*
[c] *Institute of Earth, Ocean, and Atmospheric Sciences, Rutgers, The State University of New Jersey, New Brunswick, New Jersey*
[d] *Escuela de Física, Universidad de Costa Rica, San José, Costa Rica*
[e] *Centro de Investigación en Contaminación Ambiental, Universidad de Costa Rica, San José, Costa Rica*
[f] *Departamento de Geociencias, Universidad Nacional de Colombia, Bogotá, Colombia*
[g] *Department of Atmospheric Sciences, University of Hawai'i at Mānoa, Honolulu, Hawaii*

(Manuscript received 1 February 2025, in final form 21 August 2025, accepted 9 September 2025)

ABSTRACT: The Organization of Tropical East Pacific Convection (OTREC) experiment took place from 5 August to 9 October 2019 in Costa Rica, with additional measurements collected in July and August of 2022. To observe the interaction of tropical easterly waves (TEWs) with the diurnal cycle over Central America and to assess the wave vertical structure over land, we installed a network of 15 global positioning system receivers with meteorological packages (GPS-Met), as well as two radiosonde sites, from the Caribbean to the Pacific coast. An outgoing longwave radiation (OLR)-based wave index indicates that 13 TEWs passed over the surface network during OTREC, with an additional 15 waves during 2022. The relative phasing of peak GPS column precipitable water vapor (PWV) with peak rainfall, together with vertical velocity and moisture profiles of wave active phases from reanalyses, suggests that isolated convective systems with lower-tropospheric heating and moisture evolve into more organized convective systems with elevated heating and moistening as the wave's active phase progresses inland over Costa Rica. The signatures of propagation in rainfall, PWV, and cloud-top temperature are most pronounced for the active phase, with rain events observed to propagate westward across the network with about a 12-h lag from coast to coast. In contrast, local diurnal land–sea-breeze interactions with strong surface heating play an important role in the timing of convection during the suppressed phase.

SIGNIFICANCE STATEMENT: The results of this study shed light on how tropical easterly waves, westward-propagating disturbances observed over tropical latitudes, interact with the diurnal cycle in rainfall, land–sea-breeze circulations, and low- and midlevel easterly winds over Central America, enhancing the frequency and amount of rainfall and modulating its timing over the region. These results not only highlight the importance of scale interactions in rainfall processes for tropical land areas with strong oceanic influences but also provide situational awareness to operational forecasters tasked with predicting local-scale impacts of synoptic weather events.

KEYWORDS: Convection; Atmospheric waves; Synoptic-scale processes; Water vapor; Diurnal effects; Tropical variability

1. Introduction

Tropical easterly waves (TEWs) are westward-propagating disturbances with time scales of 4–6 days and spatial scales of 2000–3000 km in the Caribbean and far eastern Pacific regions (e.g., Nitta and Takayabu 1985; Serra and Houze 2002). These waves have long been recognized for their role as incipient disturbances for tropical cyclogenesis in the east Pacific basin (Landsea 1993; Avila and Pasch 1995) and overall enhanced low-level vorticity and associated optically thick cloud anomalies across Mexico, the Caribbean, Central America and northern South America, and the far eastern Pacific during boreal summer (e.g., Roundy and Frank 2004; Kerns et al. 2008; Serra et al. 2008; Hollis et al. 2024). Western Hemisphere TEWs are among the main contributors to rainfall across the tropical Americas from June through November (e.g., Méndez and Magaña 2010; Maldonado et al. 2013; Amador and Alfaro 2014; Dominguez et al. 2020), with implications for extreme precipitation and water resource management in the region. For Costa Rica specifically, the role of TEWs in modulating seasonal precipitation patterns is critical for agricultural planning, while their associated heavy precipitation can lead to dangerous flooding. Gaps in understanding how TEWs modulate regional precipitation frequency and intensity is a serious limitation for early warning systems that protect citizens and help prepare for TEW-related heavy rain events.

Supplemental information related to this paper is available at the Journals Online website: https://doi.org/10.1175/JCLI-D-25-0067.s1.

Corresponding author: Yolande L. Serra, yserra@uw.edu

DOI: 10.1175/JCLI-D-25-0067.1

Most of our understanding of TEWs over the Caribbean–east Pacific sector has been gleaned from observations and reanalyses over open ocean (e.g., Molinari et al. 1997; Serra and Houze 2002; Petersen et al. 2003; Serra et al. 2008, 2010; Rydbeck and Maloney 2015; Whitaker and Maloney 2018; Torres et al. 2021; Hollis et al. 2024), with comparatively little focus on their effects on land precipitation, including the surface rainfall distribution and amount and intensity they produce over land in this region. One such study by Dominguez et al. (2020) found that TEW activity over Central America and northern South America contributes as much as 50% to the annual rainfall over Central America and northern South America. In a more recent study, Wiggins et al. (2023) demonstrated how TEWs modulate the diurnal cycle of rain over the Central Valley of Costa Rica, primarily by increasing the frequency of afternoon rainfall, while the mean intensity of rain is comparable to suppressed wave periods, albeit with some hint of different diurnal cycle phasing. Together, these results suggest that TEWs increase annual rainfall totals over Central America primarily by increasing the frequency of rain when it is generally favored within the diurnal cycle rather than overshadowing the diurnal forcing by the land surface, as noted by Wiggins et al. (2023). While these previous studies indicate a significant impact of TEWs on rainfall accumulations over land in part through interactions with the diurnal frequency of rain, the present study explores the nature of the mechanisms through which these synoptic–diurnal interactions occur and if these modulations are consistent across the region, including coastal and inland mountain and valley areas. The influence of TEWs on the precipitation diurnal cycle has implications for soil saturation conditions that lead to flooding and landslides and for local surface processes that modulate precipitation recycling, evapotranspiration rates, and surface–atmosphere coupling.

Prior studies of TEWs have yet to clarify the type and characteristics of convection coupled to TEWs, limiting our understanding of their impact on local rainfall and its diurnal development. For instance, using satellite rainfall, brightness temperature, precipitable water vapor (PWV), and precipitation feature categories, along with reanalysis divergence and PWV, Yasunaga and Mapes (2012a,b) classify the convective organization associated with convectively coupled equatorial waves (CCEWs), including TEWs. Their results indicate that TEWs exhibit weak midlevel divergence, which is not expected to favor mesoscale convective systems (MCSs) (e.g., Mapes and Houze 1995), and that TEW peak PWV lags peak rainfall, consistent with isolated convective systems occurring in an existing drier large-scale environment (Holloway and Neelin 2010). Based on these results, Yasunaga and Mapes (2012a) reason that TEWs are coupled primarily to isolated deep convection and not MCSs. These authors also offer an alternative interpretation that TEWs favor the initial, isolated convective period within the convective life cycle that also includes more mature stratiform cloud areas and MCSs, with the time spent in this later stage of development shorter for TEW disturbances.

In contrast, a study by Cheng et al. (2023) finds that the frequency and size of MCSs increase, as does the likelihood of heavy rain and lifetime total rainfall associated with MCSs, in the presence of CCEWs, with Kelvin and TEWs having the greatest impact on these results. In addition, Huaman et al. (2021) found that TEWs over the far eastern Pacific during the 2019 Organization of Tropical East Pacific Convection (OTREC) field campaign exhibited enhanced isolated deep convection the day before peak wave convective activity, while enhanced MCS activity was observed on the peak day itself. These results are consistent with an earlier study by Petersen et al. (2003), who found isolated deep convective rain ahead of the TEW trough and more mature stratiform rain with larger area-averaged rain rates behind the trough for waves observed during the east Pacific Investigation of Climate process study (Raymond et al. 2004). Both Huaman et al. (2021) and Petersen et al. (2003) suggest a continuum of the convective life cycle within a TEW envelope, allowing for isolated convection to be favored over the more mature stratiform regime within the full MCS life cycle suggested by Yasunaga and Mapes's work. The apparent discrepancy in MCS activity within a TEW between Yasunaga and Mapes (2012a,b) and Cheng et al. (2023), both global studies of CCEWs using similar cloud-top temperature-based algorithms for the identification of CCEWs, may also indicate that reanalysis dynamic and thermodynamic fields are not well correlated with satellite-based MCS identification algorithms. Targeted in situ measurements and comparison of various MCS tracking routines are needed to resolve such discrepancies.

The present study makes use of the OTREC Surface global positioning system receivers with meteorological packages (GPS-Met) Network and radiosonde launches on the Caribbean and Pacific coasts of Costa Rica, as well as gridded satellite and reanalysis datasets for the 2019 and 2022 rainy seasons to investigate the impact of TEWs on rainfall, PWV, and local convective instability indicators over the region, including the impacts of TEWs on the diurnal cycle of rainfall and related parameters across our network. The ultimate goal of this study is to describe the TEW vertical structure over Costa Rica for comparison with the open-ocean wave structure reported in the literature. Another goal of this study is to describe the modulation of the diurnal cycle across Costa Rica by TEWs and to identify local processes that may contribute to the observed modulation through synoptic–diurnal scale coupling.

2. Data and methods

a. *OTREC data*

Data for this study were collected by 15 surface meteorological stations across Costa Rica with collocated GPS receivers for the calculation of PWV (Fig. 1, Table 1) (Serra et al. 2020a). These GPS-Met stations were installed as part of the OTREC process study, which covered the period from 5 August to 9 October 2019 (Fuchs-Stone et al. 2020). The meteorological stations measured nominally 1-min surface pressure, air temperature, relative humidity, and wind speed and direction, and 5-min precipitation, with downward solar

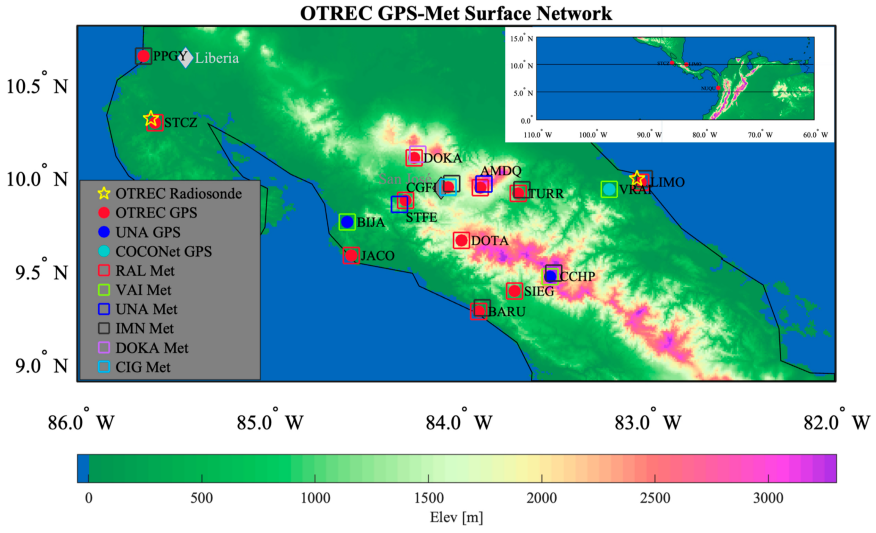

FIG. 1. Locations of OTREC upper-air stations (STCZ, LIMO) and GPS-Met stations in Costa Rica overlaid on a terrain map. GPS receivers are indicated by dots, while meteorological packages are indicated by open squares. Symbols are offset for readability. Most sites had more than one meteorological package. The inset shows broader OTREC study area with red dots marking radiosonde locations including Nuquí in Colombia. Lines at 5° and 10°N indicate the latitude range for our TD index (see text for details), while the longitude range matches that of the time–longitude section shown in Fig. 3.

radiation also available for some sites. Quality-controlled high-frequency observations from 2019 were smoothed to 5-min intervals, while data collected at lower frequencies than 5 min were interpolated to this interval, as described by Serra et al. (2020a). In addition, during OTREC, radiosondes were launched twice daily (0000 and 1200 UTC; local time is UTC-6) at STCZ (Sentić 2020) and LIMO (Serra et al. 2020b) on the Pacific and Caribbean coasts of Costa Rica, respectively (Fig. 1). The STCZ site used iMet-4 radiosondes manufactured by InterMet (iMet) Systems, while DFM-09 radiosondes manufactured by Graw were used at LIMO. A short period of 3-hourly launches occurred at LIMO from 12 to 18 September 2019. STCZ also launched more than twice daily on several days throughout September, including a period from 2 to 8 September 2019, during which 6–7 daily launches were performed. These high-frequency launch periods captured the diurnal cycle of vertical structure at the coasts. An additional radiosonde site along the northwest

TABLE 1. OTREC surface meteorological and GPS station locations, elevations, and sampling frequency for 2019.

Site ID	Latitude (°)	Longitude (°)	Elevation (m)	Sampling frequency
AMDQ	9.9341	−83.8739	2506	5 min
BARU	9.2704	−83.8834	13	1 min (Met), 5 min (rain)
BIJA	9.7499	−84.5771	545	5 min
CCHP	9.4567	−83.5048	3336	2 min (Met), 5 min (rain)
CGFI	9.9362	−84.0447	1224	5 min, hourly (winds)
DOKA[a]	10.0936	−84.2239	1257	30 and 1 min (Met), 30 and 5 min (rain)
DOTA	9.6505	−83.9723	1550	1 min (Met), 5 min (rain)
JACO	9.5698	−84.5549	9	1 min (Met), 5 min (rain)
LIMO[b]	9.9627	−83.0249	5	2 and 1 min (Met), 2 and 5 min (rain)
PPGY	10.6418	−85.6551	6	2 min, no rain
SIEG	9.3797	−83.6914	766	1 min (Met), 5 min (rain)
STCZ	10.2837	−85.5952	41	1 min (Met), 5 min (rain)
STFE[c]	9.8654	−84.2681	996	30 min, 1 min (winds)
TURR	9.9031	−83.6731	613	1 min (Met), 5 min (rain)
VRAI	9.9248	−83.1906	427	5 min

[a] DOKA Met used when RAL is not available.
[b] RAL Met used before 9 May 2019, IMN otherwise.
[c] The UNA Met station at STFE was in Puriscal, 4.3 km to the southwest of the GPS site. RAL winds are used for this site when available.

coast of Colombia at Nuquí (see Fig. 1 inset) was also part of the OTREC radiosonde network (Mejía et al. 2021) but is out of the region of focus for this study.

Due to a delay in the start of OTREC in 2019, approximately 50 radiosondes remained at the end of the field campaign. Once COVID-19 field work restrictions were lifted in Costa Rica, these extra radiosondes, along with additional sondes funded by the University of Costa Rica and Rutgers University, were launched twice daily in 2022 from 0000 UTC 29 July to 1200 UTC 10 August at STCZ and from 1200 UTC 31 July through 0000 UTC 12 August at LIMO. Hourly surface meteorological data at LIMO, STCZ, TURR, and CGFI for 2022 were provided by the Instituto Meteorológico Nacional (IMN), while 1-min surface meteorological and GPS signal delay data at VRAI were also available for 2022 from University NAVSTAR Consortium (UNAVCO). The 1-min delays were processed using the methodology described in Serra et al. (2020a) for OTREC 2019 data to obtain 1-min PWV at VRAI for the 2022 period. The 2022 surface meteorological data for the five sites were fit to a 5-min time series as in Serra et al. (2020a). While surface meteorological data in 2022 were available throughout the year, a 2022 observing period of 26 July–9 October was chosen to capture all 2022 TEW events (section 2c) and radiosonde launches, as well as to match the end date of OTREC 2019.

Soundings from the long-term World Meteorological Organization site in San José in the Central Valley region about 15 km west-northwest of San José were also collected during OTREC in 2019. However, launches were at 1200 UTC and only on weekdays, with no launches in 2022, so they are not used for this analysis. These data, along with all OTREC radiosonde and aircraft dropsonde data (Fuchs-Stone et al. 2020), did go into the Global Transmission System (GTS) and thus provide valuable constraints for the reanalyses used for portions of this study (see next section).

b. Additional datasets

The National Oceanic and Atmospheric Administration (NOAA) *GOES-16* Advanced Baseline Imager (ABI) level 1b channel 16 (13.27 μm) radiances at 2-km resolution were used in this study to characterize the cloud-top temperatures (CTTs) at our GPS-Met sites. These data are available approximately every 10 min over Costa Rica during OTREC 2019 and 2022 and were downloaded from the NOAA Comprehensive Large Array-Data Stewardship System (CLASS) and Amazon Web Services (AWS) sites. Radiances were converted to brightness temperatures using the equation provided in the product information document (https://www.goes-r.gov/users/docs/PUG-L1b-vol3.pdf), with brightness temperatures interpolated to each of our GPS-Met sites and to 5 min to match the frequency of surface meteorological data.

The fifth generation European Centre for Medium-Range Weather Forecast atmospheric reanalysis (ERA5, Hersbach et al. 2020) is used to provide additional information on the synoptic waves present during OTREC. ERA5 pressure level data are available at hourly time steps on a 0.25° × 0.25° grid from the Copernicus Climate Change Service (C3S) Climate Data Store (CDS) (Hersbach et al. 2023). The nearest grids in hourly pressure level data are selected to match the radiosonde sites at LIMO and STCZ for direct comparisons. A cross section from ERA5 is also extracted to examine the convective vertical structure coupled to the waves in ERA5 as they pass over our surface network. The western and eastern extents of the cross section are chosen to include the mean longitudes of OTREC aircraft missions in 2019, which were approximately 87°W over the eastern Pacific (EPAC) and 81°W over the Caribbean Sea (CARI) (Fuchs-Stone et al. 2020).

c. Synoptic wave identification

To characterize TEW activity during OTREC, we used space–time filtered twice-daily OLR from 1979 to 2022 on 2.5° spatial grids from the NOAA Physical Sciences Laboratory (PSL) (Liebmann and Smith 1996). The "tropical disturbance (TD)" space–time filter isolates westward wavenumbers 6–20 and periods of 2–5 days, which have been shown to represent TEW convective anomalies (e.g., Wheeler and Kiladis 1999; Serra et al. 2008, 2010). A similar approach is used to identify Kelvin waves during OTREC, as these waves are also present in the region during boreal summer and are associated with active and suppressed convective periods (e.g., Straub and Kiladis 2002; Roundy and Frank 2004). The Kelvin wave ("KEL") filter isolates eastward wavenumbers 1–14 and periods of 2.5–17 days for equivalent depths of 8–90 m (Kiladis et al. 2009). Kelvin waves are identified to confirm that variability in the TD band is dominated by TEWs alone rather than combined Kelvin–TEW events such as the one reported by Serra and Houze (2002) in the tropical eastern Pacific. As shown in Figs. 2 and 3, this is generally the case.

All TEW phases are defined with respect to the TD OLR anomalies averaged from 5° to 10°N and interpolated to the longitude of LIMO (Fig. 2). As indicated by the solid and checkered-filled areas associated with the TD OLR prepared in this way shown in Fig. 2, assignment of TEW active or suppressed phases requires these TD OLR anomalies to exceed one standard deviation (σ), or ± 10 W m^{-2}, where the standard deviation is calculated based on 5°–10°N averaged TD OLR interpolated to LIMO for July–October of 2019 and 2022. Neutral TEW periods are those for which the magnitude of these TD OLR anomalies is within $\pm 0.75\sigma$, providing separation between the active and suppressed phases and the neutral periods. Our "TD index" is defined as 1 for active periods, -1 for suppressed periods, and 0 for neutral periods. From Fig. 2, rain events exceeding 10 mm h^{-1} at the LIMO site are associated with three of the four active periods depicted for 2019, including the combined TEW and Kelvin wave active phase on 15–16 September 2019 (the standard deviation of 5°–10°N averaged KEL OLR at LIMO is 9 W m^{-2}). Some rain is also observed for three of the five suppressed phases, but it is not as heavy or as long-lasting as that observed during the active phases and, in one case, 18 September, is coincident with a Kelvin active phase.

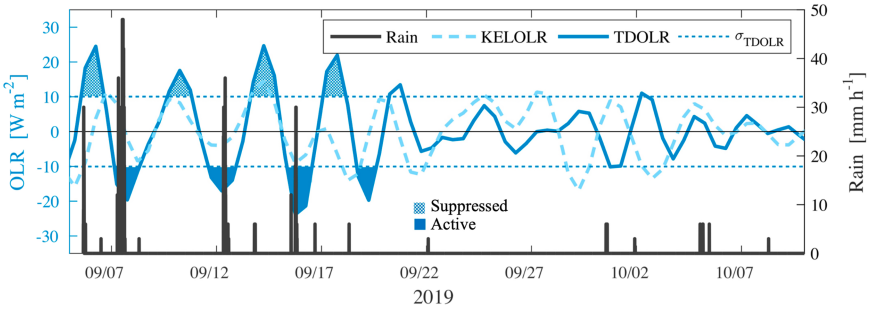

FIG. 2. Rain rate measured at LIMO together with 5°–10°N averaged KEL filtered OLR (KEL OLR) and TD filtered OLR (TD OLR) interpolated to LIMO and the standard deviation (α) of TD OLR shown for reference. Checkered (solid) filled regions indicate suppressed (active) TEW phases. The TD OLR prepared in this way defines our TD index used by this study to define TD events within our dataset. See text for details.

3. TEWs over Costa Rica during OTREC

The subseasonal variability from 26 July to 9 October included 13 easterly wave envelopes in TD OLR across Costa Rica in 2019 and 15 in 2022 (Fig. 3). Nine Kelvin waves with negative OLR anomalies over Costa Rica also traveled eastward over the region in 2019 and 2022, of which several had some overlap with negative TD OLR envelopes, at times apparently overwhelming the TD OLR signal. Of the 13 TEW negative wave envelopes in 2019, 11 were within the observing period, and of those, nine were outside the influence of Kelvin waves. Three TEW active phases in 2019 included in our study, 7 and 15 August and 16 September, were also identified by Huaman et al. (2021) for their study over the east Pacific region where OTREC aircraft flights were focused (Fuchs-Stone et al. 2020). In 2022, four of the 15 TEW active wave envelopes occurred during the radiosonde observing period, all independent of Kelvin active periods. The exclusion of Kelvin wave events from our composites does not qualitatively alter the results.

Figure 3 suggests that the degree to which TD OLR anomalies are apparent in the <20-day OLR variability fluctuates for each wave and by longitude within the 5°–10°N latitude band. For example, while the TD OLR associated with EW1 is strongly correlated with the <20-day OLR anomalies as the anomaly contours intersect within the longitudes of Costa Rica around 8 August 2019, the TD OLR contour that intersects with Costa Rica on 10 August 2019 is not as well correlated with the <20-day OLR anomalies until west of 100°W, despite the highly coherent TD OLR contour from the Caribbean Sea into the eastern Pacific. Investigation of the National Hurricane Center (NHC) surface analyses, available from the NHC online archives (NHC 2025), shows that for 4–12 August 2019, a series of tropical waves are indicated along the monsoon trough crossing Central America centered at ~10°N, consistent with our TD index and lending confidence to the TEWs captured by the TD index in this study despite the weak signal in the <20-day OLR at times within the wave envelope.

a. Mean wind vertical structure

The mean zonal and meridional wind profiles at LIMO and STCZ for the TEW active, suppressed, and neutral phases based on the waves in Fig. 3 are shown in Fig. 4. The zonal wind profiles at LIMO (Fig. 4a) indicate a midlevel easterly jetlike flow with a broad maximum from 700 to 500 hPa that is strongest when TEWs are present (active and suppressed phases) as compared to periods with no TEWs (neutral phase). The easterly jet at about 600 hPa is a persistent feature of the Caribbean–east Pacific region during June–September (Torres et al. 2021). In the context of African easterly waves, the presence of an easterly jet over West Africa has been hypothesized to favor wave development through a combined barotropic–baroclinic instability (Burpee 1972; Norquist et al. 1977; Reed et al. 1977; Thorncroft and Hoskins 1994) triggered by localized heating from transient disturbance (Thorncroft et al. 2008). Weak westerly (offshore at LIMO) flow is also apparent near the surface during all phases, possibly indicating a bias toward land breezes in the sounding data due to the launch times close to local sunrise and sunset when offshore flow is observed. Meridional winds at LIMO are overall weaker than the zonal winds at midlevels (Fig. 4b), particularly for active conditions, and consistently from the south for all phases. Below about 700 hPa, the winds become northerly, with both active and suppressed conditions having a larger magnitude than the neutral phase, increasing to a maximum near 950 hPa.

The mean zonal wind profiles at STCZ also suggest stronger winds in the presence of TEWs; however, a jetlike feature closer to 900 hPa dominates the STCZ profile, with a secondary midlevel maximum seen only during the active phase at this location (Fig. 4c). The meridional winds indicate a strong northerly component in the low-level flow at STCZ, consistent with funneling of the dominant easterly flow through the gap in the Sierra Madre mountains of southern Nicaragua and across the Gulf of Papagayo on the Pacific coast of Costa Rica, just north of our launch site at STCZ (Fig. 1). Climatologically, the Caribbean low-level jet (CLLJ) is a dominant feature in the zonal wind vertical structure over the Caribbean Sea centered at 925 hPa with a seasonal maximum in July and a seasonal minimum in October (e.g., Wang 2007; Muñoz et al. 2008). Serra et al. (2010) find a strong CLLJ favors TEW tracks across southern Nicaragua and the Guanacaste Peninsula

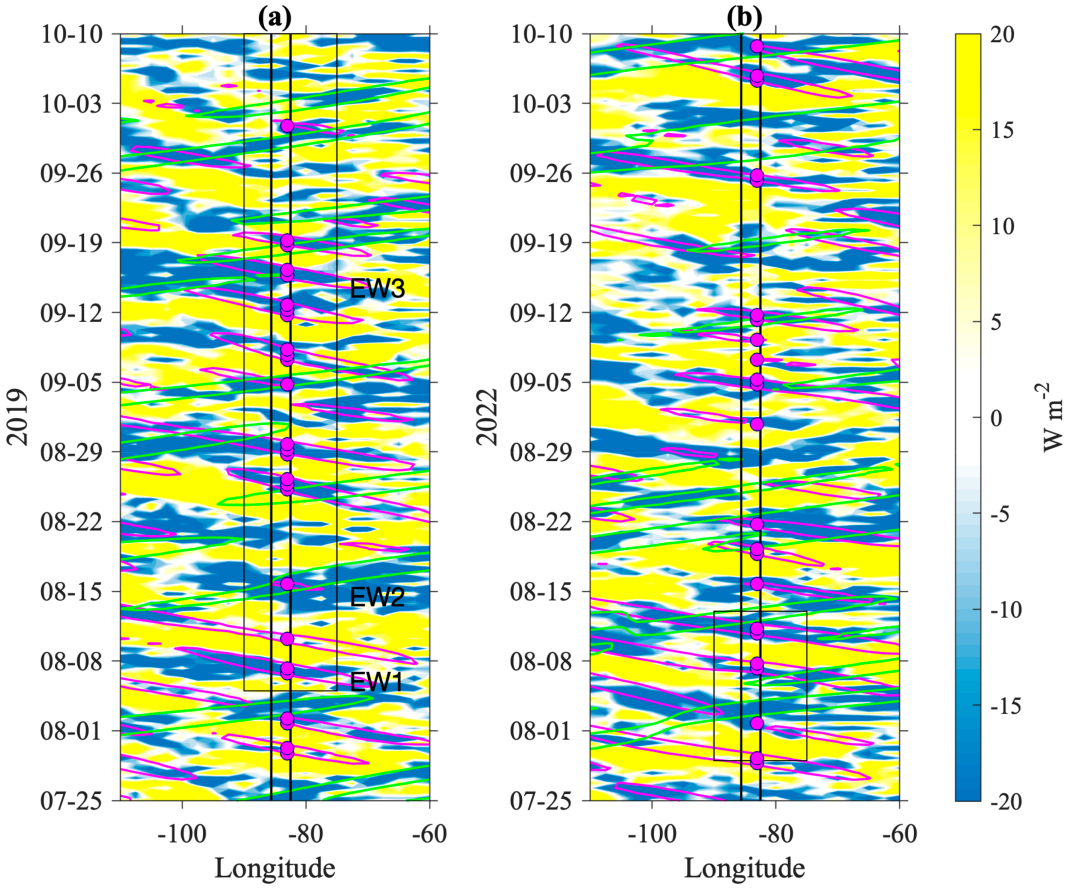

FIG. 3. The KEL OLR −9 W m^{-2} contour (light green), TD OLR −10 W m^{-2} contour (magenta), and the <20-day OLR anomalies averaged from 5° to 10°N (filled contours) for 25 Jul–9 Oct (a) 2019 and (b) 2022. TD OLR negative anomalies at LIMO that meet the TEW active event criteria are shown as magenta dots (TD index = 1). The OTREC radiosonde observing periods are highlighted by black rectangles. The period shown corresponds to the full 2022 surface meteorological dataset, while the 2019 surface meteorological dataset nominally begins on 5 Aug and goes to the end of the period. EW1, EW2, and EW3 indicate the TEWs identified by Huaman et al. (2021) for reference.

and out along the ITCZ, south of and more longitudinal than the typical track for east Pacific TEWs during boreal summer. Whitaker and Maloney (2018) show similar results, with enhanced low-level relative vorticity shifted south over Nicaragua and northern Costa Rica for their strong CLLJ composites. These studies additionally suggest that TEWs can be more active during strong CLLJ phases. Interestingly, like LIMO, STCZ also shows stronger easterly flow near 600 hPa during TEW active phases, again consistent with a possible role for the midlevel easterly flow in TEW activity over Costa Rica during OTREC, as discussed in Torres et al. (2021).

b. *OTREC TEW vertical structure*

The vertical structure of TEWs based on OTREC soundings is shown in Fig. 5 for STCZ and LIMO. The TEW structure is represented here by vertical composites of active phase 2–10-day anomalies shown as a function of lag, where lag 0 marks the start of the TD phase for the twice-daily TD index at LIMO. Negative lags represent TEW anomalies that have moved west of LIMO relative to lag 0, while positive lags represent anomalies arriving from the east. Compositing the vertical profiles at STCZ with respect to the TD index at LIMO results in about a 12-h shift in peak wave activity from that seen at LIMO, as evidenced by the lag in the twice-daily TD OLR and radiosonde-derived PWV at STCZ (Figs. 5a,b). In addition, while the peak PWV anomalies at LIMO are collocated with the peak negative TD OLR anomalies, peak PWV lags the peak TD OLR anomalies at STCZ and has a weaker modulation by the TEW than at LIMO. The lag of PWV with respect to the peak in deep clouds at STCZ and the smaller PWV anomalies suggest a lack of organized convection at this site. We return to this idea again when we present ERA5 vertical velocity anomalies below.

The temperature anomalies at LIMO for the active TEW phase indicate a bimodal structure with cold anomalies below 500 hPa and warm anomalies extending above this level up to about 200 hPa (Fig. 5h) from lags −0.5 to +1.0 days when the

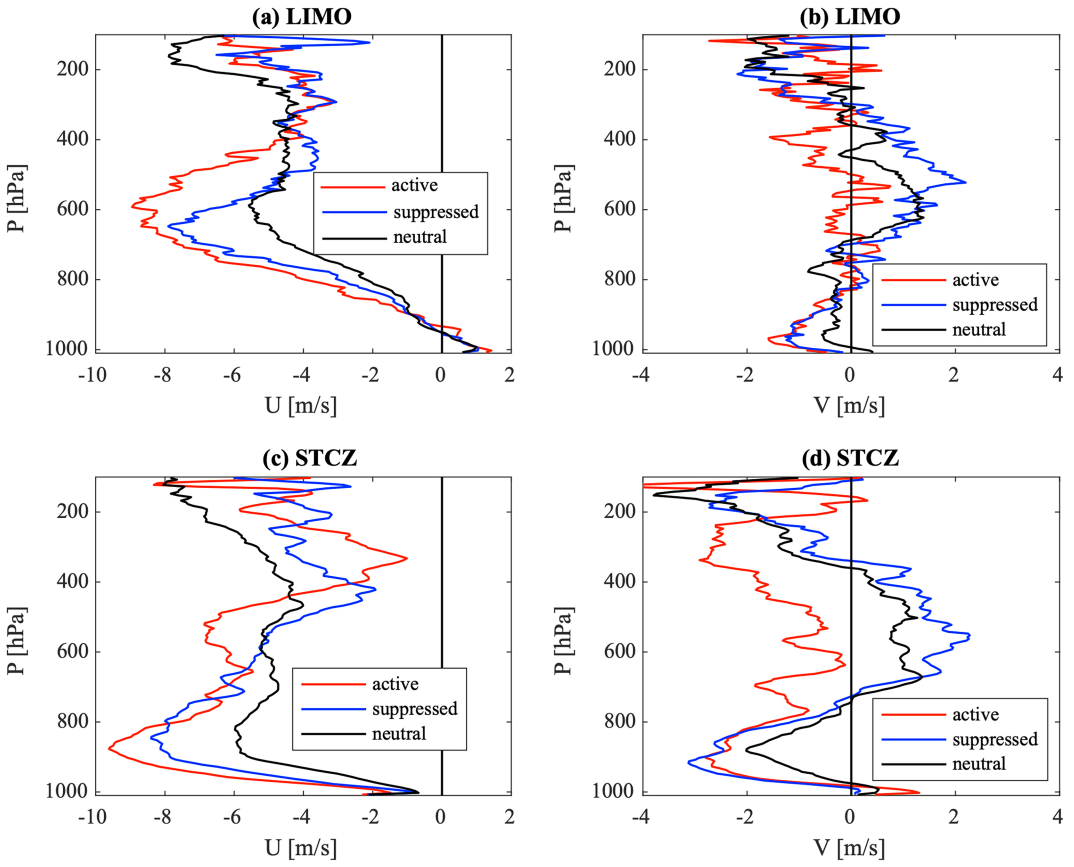

FIG. 4. Mean (a) zonal and (b) meridional wind at LIMO for the active, suppressed, and neutral TD wave phases. (c),(d) As in (a) and (b), but for STCZ.

TD OLR is most negative (Fig. 5f). During peak TEW wave activity, moisture anomalies (Fig. 5i) are in phase with the bimodal temperature structure at this location and indicate an elevated heating profile coincident with the TEW convective activity. At negative lags, moist anomalies are seen at low levels, further suggesting a buildup of boundary layer moisture during preactive periods, which is often associated with shallow convection.

The temperature and moisture anomalies at STCZ (Figs. 5c,d) look considerably different from those at LIMO. For lags 0–1.0 day, when the TD OLR is most negative at this location (Fig. 5a), cold rather than warm anomalies from 800 to 400 hPa align with positive moisture anomalies, indicating weak convection–wave coupling. Moist anomalies at low levels are also seen at positive rather than negative lag with respect to the active phase (Fig. 5d), in contrast to LIMO (Fig. 5i), indicating a lack of shallow to deep convective development. Overall, the temperature and moisture anomalies seen at STCZ differ from the results of Serra et al. (2008, 2010) for Caribbean and Pacific TEWs and from profiles of temperature and humidity anomalies for convectively coupled waves more generally (e.g., Kiladis et al. 2009). Thus, while there is a large-scale TD OLR anomaly and associated PWV anomaly at this location consistent with a TEW active phase, a clear convective signal that suggests convection–wave coupling does not appear to be present at STCZ.

Wiggins et al. (2023) also performed a long-term climatological wet-season TEW vertical structure analysis for the WMO sounding site in the Central Valley of Costa Rica. Their lead–lag temperature and moisture profiles are more similar to the behavior shown here for LIMO than for STCZ, although the elevation of the WMO sounding site (921 m MSL; base sounding pressure of ~900 hPa) means that some of the very low-level features in the OTREC soundings are absent.

The zonal and meridional wind anomalies at both LIMO and STCZ indicate a northeasterly flow ahead of the active phase to the west (negative lag) and a southwesterly flow behind the active phase to the east (positive lag) in the midtroposphere, consistent with the circulation around a low pressure system. At LIMO, the meridional wind anomaly profiles tilt toward positive lag from about 550 to 400 hPa and toward negative lags from 400 to 200 hPa. The tilt of the wave axis with height is opposite the mean zonal shear at these levels (Fig. 4a) and is thus consistent with baroclinic energy conversions from the mean flow to the wave as found for African

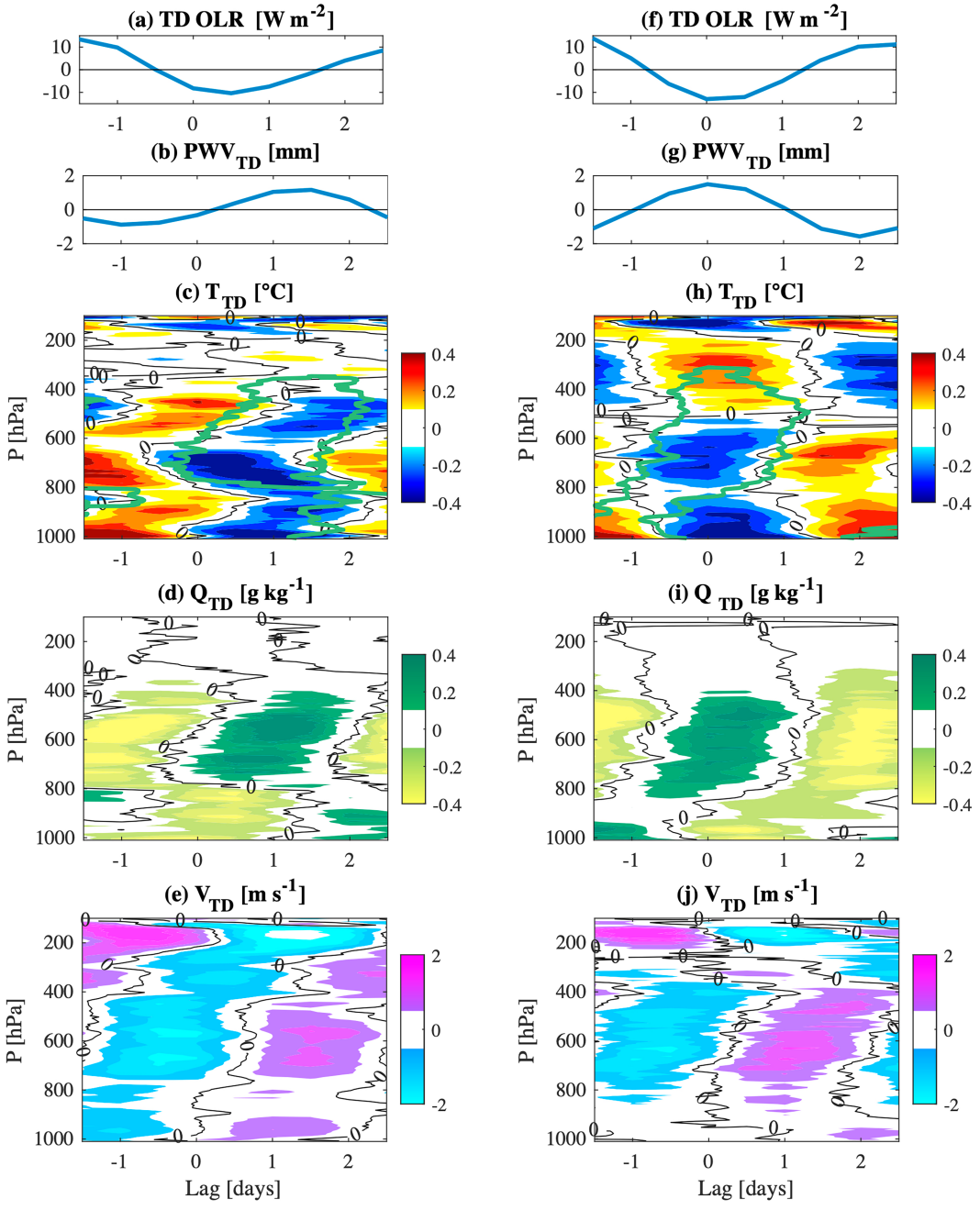

FIG. 5. Active phase (a) TD OLR and 2–10-day anomalies in (b) PWV, (c) air temperature, (d) mixing ratio, and (e) meridional wind at STCZ for the 2019 and 2022 OTREC radiosonde periods vs lag. The $+0.1$ g kg^{-1} mixing ratio contour from (d) is contoured in green in (c). (f)–(j) As in (a)–(e), but for LIMO. The lags at STCZ are shifted to center the minimum in TD OLR at this location. The TD subscript indicates 2–10-day filtered variables; soundings at 0000 and 1200 UTC are used for these composites.

waves near 10°N (Reed et al. 1977). A similar tilt in the wave axis above 550 hPa may also be present at STCZ, although it appears less pronounced than at LIMO.

The evidence for momentum transfer from the mean vertical zonal wind shear to eddy energy at LIMO and, to a lesser extent, STCZ associated with the easterly jetlike feature at 600 hPa is evidence for a link between TEWs and this dynamic feature over the region as hypothesized by Torres et al. (2021). The collocation of positive temperature and moisture anomalies typically found associated with TEWs (e.g., Serra et al. 2008, 2010; Whitaker and Maloney 2018) is consistent with the conversion of eddy available potential energy from

the latent heating of convection to eddy kinetic energy, a dominant energy source of TEWs in the east Pacific according to these studies. Examination of the positive moisture anomalies (Fig. 5h, red contour) collocated with the dipole in temperature anomalies (Fig. 5h, filled contours) during the active phase of TEWs in OTREC at LIMO supports these results, while the positive moisture anomalies collocated with cold temperature anomalies aloft at STCZ (Fig. 5c, red contour encompassing blue filled contours) are not consistent with the conversion of eddy available potential to kinetic energy at this location during OTREC. In the next section, we will use ERA5 to explore the relationship between convection and TEWs across Costa Rica further.

c. *ERA5 omega vertical structure*

ERA5 2–10-day anomalies in vertical velocity and temperature averaged latitudinally across Costa Rica from 9° to 10.25°N are shown in Fig. 6. Our radiosonde sites at LIMO and STCZ, as well as the GPS-Met site at CGFI in the Central Valley, and the approximate mean longitudes for the OTREC aircraft missions over the EPAC and CARI are indicated by blue dots in Fig. 6 for reference. As in Fig. 5, ERA5 composites are relative to the TD index at LIMO, resulting in a shift of the wave-related anomalies to the west at positive lags. While the ERA5 0000, 0600, 1200, and 1800 UTC profiles are composited here, limiting the composites to 0000 and 1200 UTC, as in Fig. 5, yields similar results (not shown).

The ERA5 temperature anomalies across Costa Rica are in good overall agreement with the OTREC observations at LIMO (Fig. 5h), with cold anomalies in the lower troposphere and warm anomalies aloft as the wave convective phase, indicated here by the warm colors in vertical velocity, pass over the region. Since these observations, as well as all other OTREC radiosonde and aircraft dropsonde data collected over the Caribbean Sea and east Pacific (Fuchs-Stone et al. 2020), were sent to the GTS, they likely provided added constraints to the profiles presented in Fig. 6.

Anomalous upward motion over the CARI has a lower-tropospheric maximum near 850 hPa starting around lag −1, suggesting that shallow and/or bottom-heavy isolated convection precedes the active phase (Fig. 6a). By lag −0.5, the vertical motion extends above 500 hPa at this location, although peak values persist at low levels (Fig. 6b). Cold temperature anomalies appear in the boundary layer and extend into the lower troposphere, consistent with the growth from shallow to deep convection and the formation of downdrafts, while warm anomalies are seen to develop aloft with the deepening convection. The collocation of upward motion with the warm anomalies aloft suggests a coupling between the convection and the wave. By lag 0, upward motion at CARI is top-heavy, indicating the dominance of stratiform convection (Schumacher et al. 2004). By lag +0.5, this top-heavy structure is weakening as the main updraft region moves further west over the central and then western slopes of Costa Rica from lag 0 to lag +0.5 days.

Over the land, shallow upward motion is also seen at LIMO ahead of the arrival of the wave active phase at lag −1,

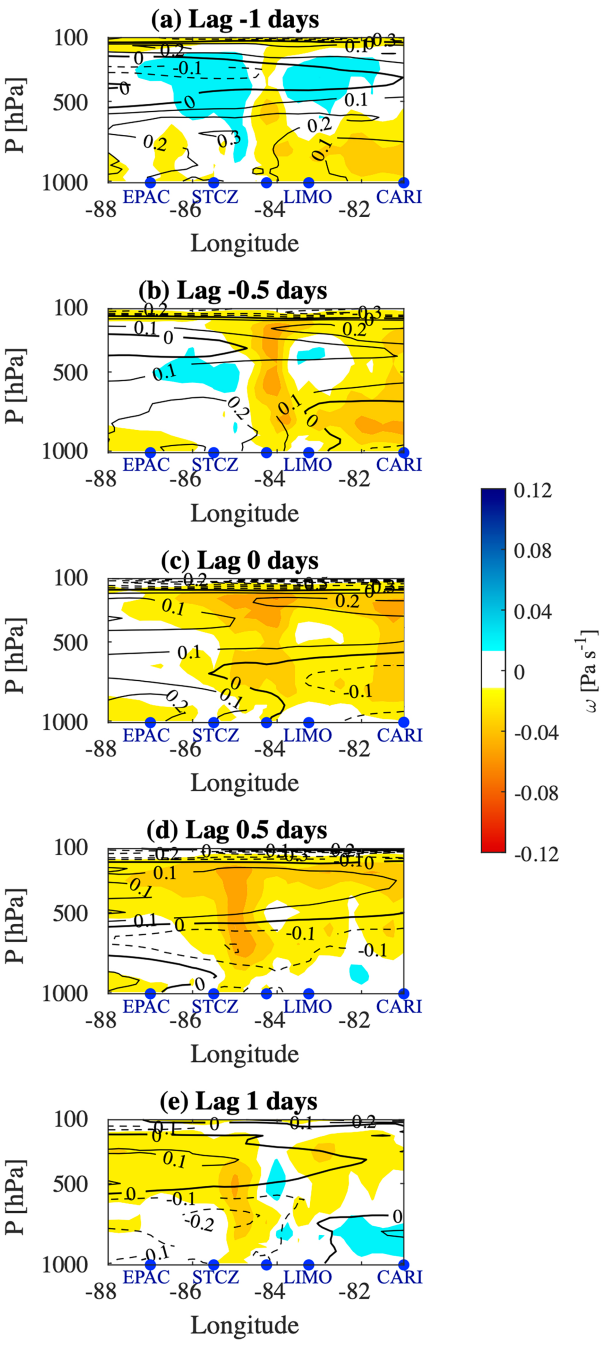

FIG. 6. Lagged ERA5 2–10-day anomalies in vertical velocity (shaded) and temperature (contours) averaged from 9° to 10.25°N for (a) lag −1, (b) lag −0.5, (c) lag 0, (d) lag +0.5, and (e) lag +1 days vs height composited for active periods of the TD index at LIMO. (from left to right) Blue dots along the x axis indicate the longitudes of EPAC, STCZ, CGFI (no label), LIMO, and CARI for reference.

while weak upward motion throughout the column is seen over the Central Valley, suggestive of diurnal and orographically driven isolated deep convection. By lag −0.5, the shallow convection at LIMO and the deep convection over the Central

Valley have both intensified, while the warm anomalies are weakening at low levels compared to the previous lag (Fig. 6b). At lags 0 and +0.5 (Figs. 6c,d), the peak active phase at LIMO, anomalous upward motion is seen near 750 hPa, in a region of cool anomalies, as well as near 250 hPa, in a region of warm anomalies, suggesting that latent heating due to convection may provide energy to the waves at this time across the central and eastern portions of Costa Rica. As the waveform moves farther west (Fig. 6e), anomalous upward motion at LIMO is again collocated with cold anomalies, minimizing the efficiency of convection for wave energetics, and the intensity of upward motion subsides.

While ERA5 profiles of anomalous upward motion suggest that convection associated with the passage of a TEW trough over Costa Rica is less organized along the Caribbean coast than over the inland and mainland Pacific coast regions, anomalous upward motion does not appear to reach STCZ at any lag, except as an extension of the anomalous upward motion associated with anvils from deep convection over the Central Valley and western slopes of the mountains of Costa Rica (Fig. 1) as the wave propagates westward. This result is consistent with the OTREC soundings shown in Fig. 5, which indicate moist anomalies are not coupled to a vertical dipole structure in temperature and thus do not indicate conditions favorable for convective growth and convective coupling with the wave vertical temperature structure.

d. TEW modulation of rain events

PWV and its rate of change prior to rain onset offer insight into the temporal development and character of convective events (e.g., Holloway and Neelin 2010; Adams et al. 2011, 2015; Yasunaga and Mapes 2012a,b; Serra et al. 2020c). For instance, Yasunaga and Mapes (2012a,b) suggest that the phasing of peak PWV to rain onset can indicate whether convective or stratiform convection is present, with the former increasing PWV by moistening the environment following peak rainfall while the latter results in lowering PWV through drying of the environment supporting the convection. The rate of change of PWV can also be used as a proxy for short-term water vapor convergence in the atmospheric column, assuming that local sources from cloud water and evaporation are small (e.g., Adams et al. 2011, 2013).

To examine how TEWs affect rainfall events over Costa Rica during OTREC, we first consider a method to identify events. As a first criterion, we require events to have a 5-min rain rate exceeding 1.7 mm h^{-1}, the median rain rate for all sites. To ensure well-separated events, instances with 5-min rain rates exceeding the 1.7 mm h^{-1} threshold are further filtered to exclude occurrences of 5-min rain rates exceeding this threshold in the 6 preceding h. The end of a rain event is marked by the last 5-min value above 0.0 mm h^{-1} within the 12-h period from the start of the event. In total, 681 rain events met these criteria during OTREC. The median duration of these rain events is 30 min, with 75% of events lasting under 2 h. To obtain composites by TEW phase, the TD index within ±30 min of onset ($t = 0$) is examined, with active or suppressed values overriding neutral values within that time window. No 1-h period contains 5-min values that meet both the active and suppressed criteria in our dataset. There are 431 rain events during neutral periods, 98 during active TEW phases, and 86 during suppressed TEW phases.

Figure 7 shows the composite CTT and PWV anomalies and rain rates for rain events by TEW phase for ±48 h from rain event onset (i.e., time = 0). The rate of change of PWV over 24 h ($d\mathrm{PWV}/dt_{24\mathrm{h}}$; green triangles in Fig. 7) is estimated using a linear fit to the PWV data over 24-h intervals (represented by horizontal brackets on either side of the green triangles), shifting by 12 h and spanning ±48 h from the event start time. Over 24 h, local sources of water vapor from evapotranspiration and evaporation within clouds may be contributing to the change in PWV, along with horizontal water vapor convergence.

While a threshold of 6 h is chosen to separate rain events, all composites in Fig. 7 indicate average rates remain well below the event threshold (dotted line) for up to 12 h prior to onset, increasing in magnitude as lead times approach 24 and 48 h before and following onset, highlighting the prominent diurnal cycle in rainfall at our sites. This is especially evident for the neutral composite (Fig. 7a), which benefits from the largest number of events, resulting in a smoother rainfall curve. Using lower rain-rate thresholds or shorter times between rain events does not change the qualitative behavior shown in Fig. 7. Strong diurnal cycles are also observed in CTT and PWV in these composites. This analysis can be compared to Holloway and Neelin (2010), who analyzed in situ PWV, cloud-top height, and rainfall for Nauru, a flat, 21-km^2 island in the tropical western Pacific, with no visible diurnal cycle in rainfall or PWV seen at that location. We hypothesize that the size of the land area and its topography impact the magnitude of the diurnal cycle in PWV, similar to the results for rainfall on tropical islands (Sobel et al. 2011; Ulrich and Bellon 2019). A diurnal cycle in PWV is also observed for GPS-Met sites on the large island of Sumatra (~500 000 km^2: Torri et al. 2019) and in the tropical Amazon (Adams et al. 2011, 2015; Serra et al. 2020c). Adams et al. (2015) and Torri et al. (2019) find that the local geographic conditions and seasons impact the diurnal magnitude and phase of PWV in these regions. Torri et al. (2019) also find that an atoll offshore of Sumatra has a weak diurnal cycle in PWV, consistent with the observations at Nauru (Holloway and Neelin 2010). As will be shown in the next section, geography also impacts the local diurnal cycle across Costa Rica, demonstrating the role of the surface in modulating precipitation.

The 24-h trend in PWV for active events from 48 to 24 h prior to event onset is negative (Fig. 7b), suggesting divergence and possibly loss of moisture due to rain exceeding that of the mean at these lead times. This can be compared to neutral events, where the 24-h trend in PWV is close to zero (Fig. 7a). During the peak of the active phase, from 24 h before to 24 h following rain onset, CTT anomalies are negative or near zero, consistent with the presence of deep clouds over this roughly 2-day period. In contrast, neutral events continue to show a strong diurnal cycle in CTT over this same period surrounding event onset. The rate of change of PWV over 24 h for active events becomes positive from about 36–24 h

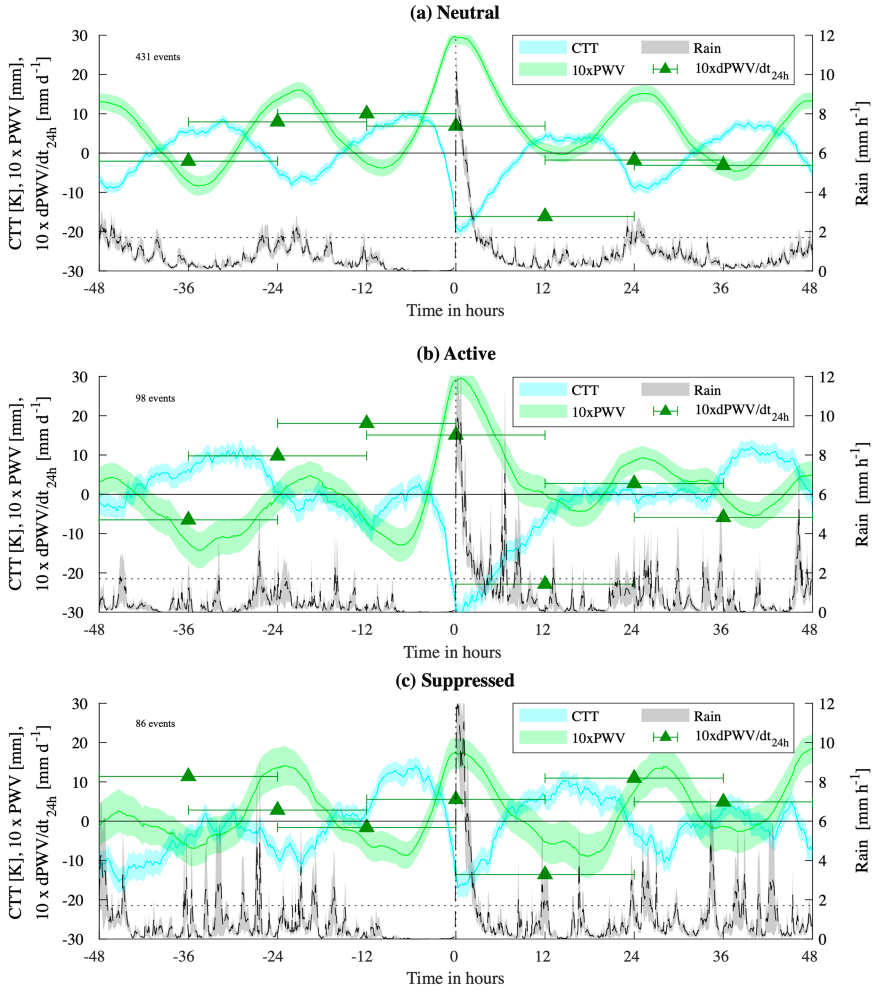

FIG. 7. Composite CTT and PWV anomalies and rain rate, along with their standard deviations (shading) for (a) neutral, (b) active, and (c) suppressed TEW rain events at all sites for both 2019 and 2022, showing ±48 h from event onset at $t = 0$. Also shown is $d\text{PWV}/dt$ (green triangles) estimated over 24 h (green brackets; see text for details). The median 1.7 mm h^{-1} rain rate (dotted black line) is shown for reference. PWV anomalies and $d\text{PWV}/dt_{24h}$ are scaled by a factor of 10 to show on the same scale as CTT anomalies. There are 431 neutral, 98 active, and 86 suppressed rain events in the combined 2019 and 2022 OTREC dataset.

prior until 12–24 h following rain onset, with peak 24-h changes of up to 2 mm d^{-1}, similar to neutral events (Fig. 7a). By 36 h from rain onset, daily changes to PWV over 24-h fall below zero similar to the 24-h trend seen 36 h prior to onset and consistent with anomalous PWV convergence during active rain events. Neutral PWV changes over 24-h show a similar pattern, but with lower amplitude suggesting that wave-related water vapor convergence is evident at our sites.

The active phase increasing trend in 24-h PWV over the 24–12 h before rain onset can be compared to the decreasing trend in this quantity seen for the suppressed phase over this same period (Fig. 7c). During suppressed conditions, a positive value in the 24-h rate of change in PWV at the 36-h lead time becomes close to zero at 24- and 12-h lead times, with a peak magnitude of only about 0.5 mm d^{-1} for the 24 h centered on the rain event. In addition, peak PWV itself remains below 2 mm compared to over 3 mm for neutral and active events. At 24 h following suppressed events, the 24-h change in PWV increases again, with a magnitude similar to that seen at 36 h prior to onset, followed by smaller but still increasing 24-h PWV at 36 h following onset. Thus, suppressed events have lower overall peak 24-h PWV increases and peak PWV values at rain onset than the days leading up to and following these phases.

The occurrence of stronger water vapor convergence 1–1.5 days prior to peak rain activity, followed by drying up to 1.5 days after the rain onset for active events, is consistent with the development of organized convection at our sites associated with TEW active phases. Similarly, the lack of water vapor convergence over 24 h for the day preceding suppressed events, followed by moistening for 1–1.5 days following rain onset, is consistent with more isolated convection occurring during

TEW suppressed phases. The roughly 24–36-h duration of the active event is also consistent with a quarter wave period of a 4–5-day TEW. Thus, we hypothesize that the modulation of PWV, CTT, and rainfall shown in Fig. 7 is at least in part associated with the passage of TEWs during OTREC and that the modulations are consistent with more organized convection occurring during the active phase of a TEW and more isolated convection occurring during the suppressed phase.

4. TEW modulation of surface parameters on diurnal time scales over Costa Rica

The diurnal cycle is an important mode of variability in tropical rainfall (e.g., Yang and Slingo 2001; Nesbitt and Zipser 2003; Liu and Zipser 2008) that can interact with lower-frequency variability in the tropics (e.g., Mora et al. 2020; Peatman et al. 2014; Ruppert and Johnson 2015). Surface buoyancy forcing related to daytime heating is a key component of the initiation of afternoon convection over tropical land areas, as demonstrated in recent studies of rainfall over Costa Rica (Mora et al. 2020; Wiggins et al. 2023). Sea breezes additionally play an important role in the diurnal cycle in rainfall near coastlines in the tropics through their influence on the propagation of peak rainfall along sea- and land breeze fronts (e.g., Yang and Slingo 2001; Sobel et al. 2011; Ulrich and Bellon 2019). To examine interactions between TEWs and the diurnal cycle, composites of variables at our sites are constructed for the active, suppressed, and neutral phases of TEWs by first interpolating the TD OLR at LIMO to 5 min to match the surface network time series and then creating a 5-min TD index by assigning the TEW phase to each 5-min value using the criteria described in section 2. Note that PPGY had no rain gauge, and BIJA lacked sufficient observations of rainfall for the active and suppressed periods, so composites of rainfall in Figs. 8–10 exclude these sites.

a. TEW modulation of the diurnal cycle in convection

To illustrate the key aspects of the TEW influence on the diurnal cycle in rainfall while increasing the statistical significance of the results, we consider diurnal composites aggregated over sites in three regions: CARIB (LIMO, VRAI; Fig. 8), INLAND (TURR, AMDQ, CCHP, DOKA, CGFI, STFE, DOTA; Fig. 9), and PACIFIC (BARU, BIJA, JACO, PPGY; Fig. 10). The approximate degrees of freedom for the composites are provided in the figure captions, where NA_{0000LT}, NS_{0000LT}, and NN_{0000LT} are for active, suppressed, and neutral air temperature data at 0000 LT, respectively. Data are averaged by local hour, and the degree of freedom is estimated as the number of days with data for a particular local hour. This number can exceed the number of campaign days as there is more than one site represented in the composite for each region. Air temperature is available at all sites, so it was used to quantify the approximate degrees of freedom; however, the degrees of freedom vary somewhat depending on the local hour, surface parameters, and region.

Figures 8–10a and 10b show composites of rain rate R and fraction of time raining (F), where the latter is an average of a binary indicator of rainfall greater than 1 mm h^{-1} in the 5-min time series, avoiding light rain and drizzle events not captured by the tipping-bucket rain gauges used at some sites. Rain intensity (average rain rate when rain is present) is not included, as there are not enough events in the OTREC dataset to provide a stable mean in this quantity for the active and suppressed phases of TEWs.

While the suppressed and neutral phase diurnal peak in rainfall rate, frequency, and PWV anomalies are in the afternoon for all three regions, active phase peaks in these quantities shift from morning at CARIB (Figs. 8a–c) to late afternoon at INLAND (Figs. 9a–c) and then early evening at PACIFIC (Figs. 10a–c). Active phases also strongly modulate surface solar radiation (RAD) at all but the PACIFIC sites (Figs. 8–10d), suggestive of the wave influence on cloud cover over the Caribbean and Central Valley of Costa Rica, with that influence being more complex on the Pacific coast, as discussed in section 3. The impact on surface parameters for each of these regions discussed next will be shown to vary as a result of the differences in the diurnal timing of convection for the TEW active phase, as well as differences in the wave signature across our network.

The active period at CARIB is characterized by lower rain rates (Fig. 8a) and warmer CTT anomalies (Fig. 8e) than that at PACIFIC (Figs. 9a,e) and INLAND (Figs. 10a,e), suggesting that the convection associated with TEWs at CARIB is likely less organized than for the other regions, consistent with the vertical velocity structure shown in Fig. 6 discussed earlier. We hypothesize that the weaker convection for CARIB, in part, results from the predawn initiation of convection at this site for active periods. However, modeling sensitivity studies would be needed to confirm the importance of the diurnal phasing on the Caribbean coast rainfall intensity. Since daytime heating of the surface is low at this time (Fig. 8g), boundary layer destabilization is likely not contributing to the invigoration of convective activity. In addition, the cloud cover from the morning convection limits surface heating over the course of the day at CARIB. This is indicated by comparing the diurnal cycles of air temperature (Fig. 8g), mixing ratio (Fig. 8h), and surface moist static energy (MSE) (Fig. 8f) with those at PACIFIC (Figs. 10g,h,f). CARIB has the smallest diurnal amplitude in these quantities, followed by INLAND (Figs. 9g,h,f), where daytime convection is also present throughout an extended period during morning hours, curtailing surface heating for this region as well. However, the magnitude of the daytime peak in these quantities is more favorable to convection for INLAND than for CARIB, and together with the arrival of the TEW peak PWV midday, may result in the overall more organized and deeper convection for this region than for CARIB.

The timing in peak cold clouds for the active phase composites is progressively later in the day from CARIB, where cold clouds peak from about 0800–1200 LT to INLAND, where peak cold clouds are from about 1300–1800 LT, and finally to PACIFIC, where peak cold clouds are from 1800 to 1900 LT.

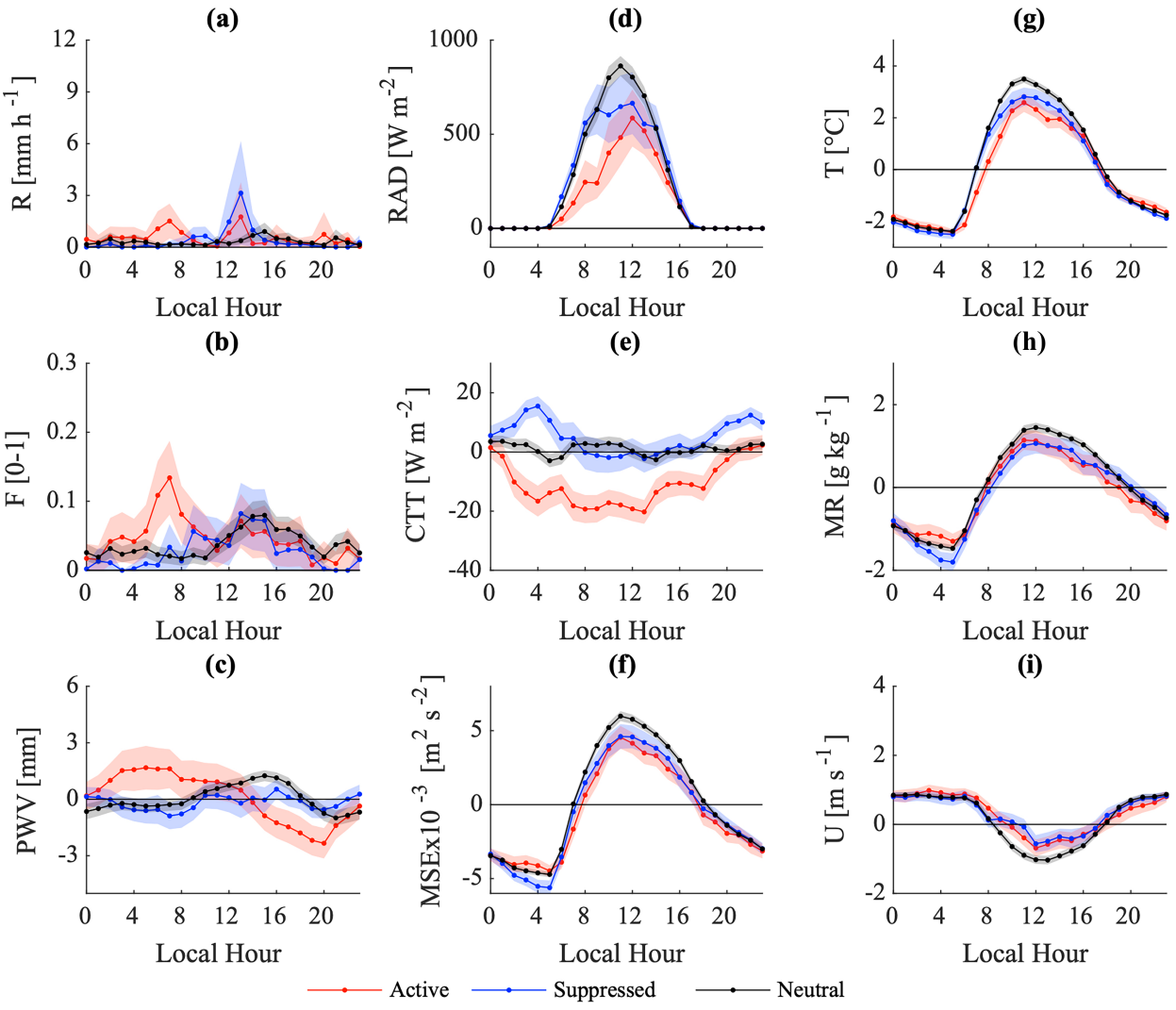

FIG. 8. The composite diurnal cycle in (a) rain rate, (b) rain frequency, (c) PWV anomalies, (d) downward solar RAD, (e) CTT anomalies, (f) MSE anomalies, (g) air temperature anomalies, (h) MR anomalies, and (i) zonal wind anomalies for the CARIB region for the active, suppressed, and neutral phases of TEWs observed by the OTREC Surface GPS-Met Network. The shading indicates the standard deviation of the mean for each hour. The number of hours with data at 0000 LT for active, suppressed, and neutral phases is $NA_{0000LT} = 34$, $NS_{0000LT} = 39$, and $NN_{0000LT} = 145$, respectively.

Peak PWV also shifts from 0300 to 0700 LT for CARIB (Fig. 8c) to 0900–1400 LT for INLAND (Fig. 9c) to 1500–1800 LT for PACIFIC (Fig. 10c). We hypothesize that the progression across the regions reflects TEW propagation across Costa Rica. PACIFIC also shows a peak in PWV near 0900 LT when the onshore flow is maximum for this region (Fig. 10i). Thus, the earlier peak in PWV anomalies for PACIFIC may be associated with sea-breeze circulations enhanced by the TEW. Of course, it is unclear why TEW troughs would be favored to arrive over Costa Rica at the east coast in the early morning, and the apparent propagation could be attributed to the native 12-h resolution of the OLR forming the wave index. However, it may also suggest that there is an optimal phasing of TEW convection with the peak diurnal cycle over the inland areas, where local diurnal forcing is strongest, resulting in the observed phasing at the east and west coasts of the country. Addressing this issue is beyond the scope of the OTREC data highlighted in this study.

b. TEW modulation of sea-breeze circulations

Composites of full zonal wind for all three TEW phases are shown in Figs. 8i–10i. The diurnal amplitude is largest for the coastal regions (CARIB and PACIFIC), while INLAND shows little to no diurnal variability. At both CARIB and PACIFIC, the zonal winds are offshore at night and onshore during the day, or westerly at night and easterly during the day at CARIB and easterly at night and westerly during the day at PACIFIC, consistent with sea-breeze circulations. At INLAND, easterly flow dominates the near-surface winds

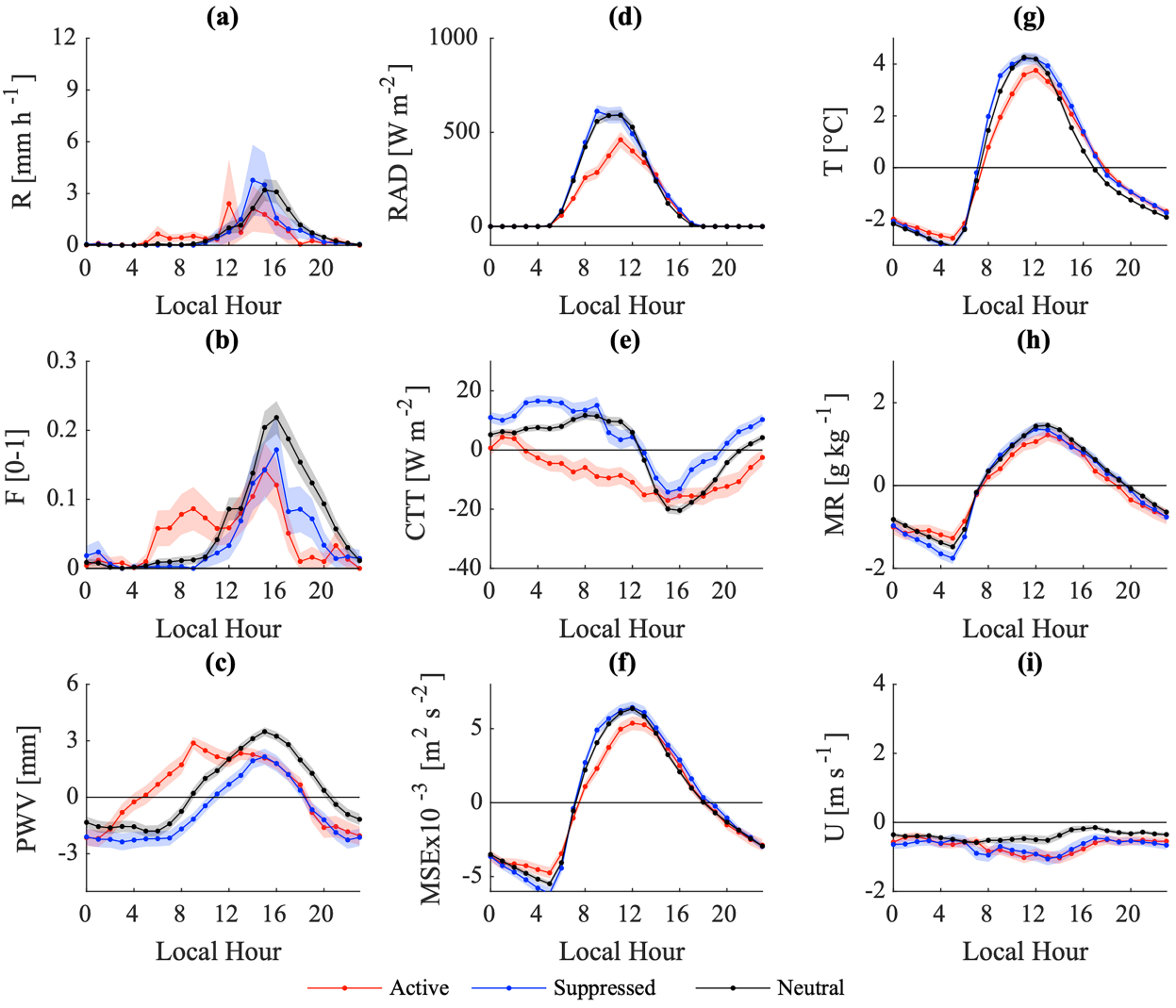

FIG. 9. As in Fig. 8, but for the INLAND region. $NA_{0000LT} = 69$, $NS_{0000LT} = 77$, and $NN_{0000LT} = 263$.

and is stronger when TEWs are present regardless of wave phase. Sea-breeze circulations are disrupted at CARIB for TEW passages when both the active and suppressed daytime amplitude in the zonal wind are reduced compared to the neutral period. The PACIFIC region sea-breeze circulations for the suppressed period are similar to that of the neutral period, but the active phase transition to easterly (offshore) flow shortly after 1000 LT is roughly in phase with the arrival of the TEW positive PWV anomalies. This disruption of the sea-breeze circulations for PACIFIC by TEWs may contribute to the delay of deep cloud development for this region, which directly follows peak onshore flow for the neutral and suppressed periods. It is also interesting to note that while the diurnal peak in near-surface mixing ratio follows the diurnal peak in air temperature, the diurnal peak in PWV follows the peak onshore flow associated with the sea breeze at both PACIFIC and CARIB. The exception to this is the active period for CARIB when the TEW and diurnal cycles are largely out of phase with one another. As a result, we find that TEW active periods appear to amplify the diurnal cycle in rainfall for the INLAND and PACIFIC sites but not the CARIB site.

5. Large-scale context for the OTREC surface network observations

In this section, we discuss the larger scale and climatological context of our OTREC surface meteorological and radiosonde observations by examining the 2019 and 2022 Caribbean to far eastern Pacific boreal summer anomalies with respect to the regional climatology. Looking first at interannual variability, ERA5 sea surface temperature (SST) and 850-hPa wind anomalies for August–September 2019 (see Fig. S1b in the online supplemental material) indicate that the far eastern Pacific was anomalously warm with easterly wind anomalies reinforcing the climatological easterly flow across the region

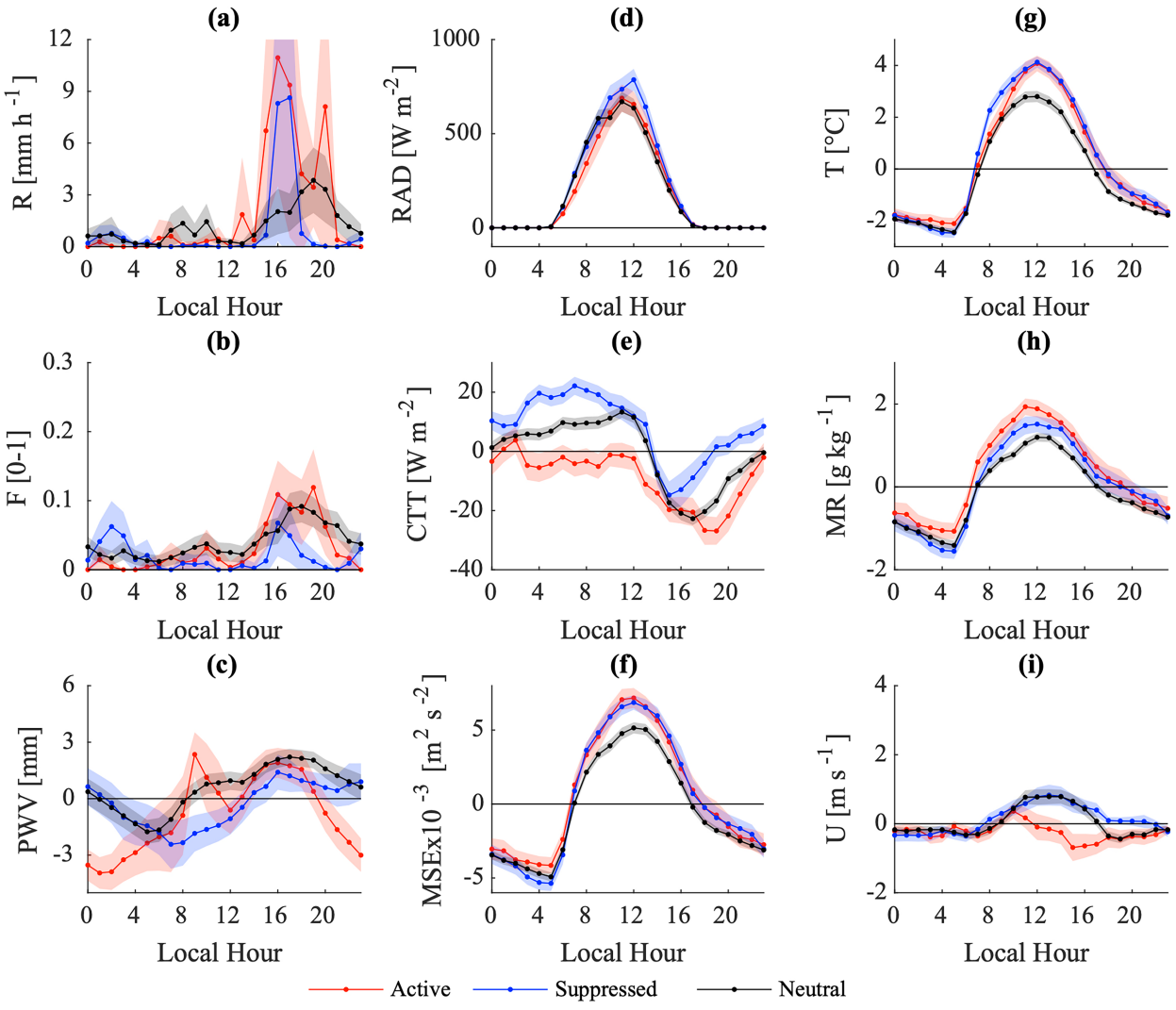

FIG. 10. As in Fig. 8, but for the PACIFIC region. $NA_{0000LT} = 22$, $NS_{0000LT} = 24$, and $NN_{0000LT} = 75$.

(Fig. S1a), while August–September 2022 was anomalously cold in the far eastern Pacific with weak westerly wind anomalies (Fig. S1c). The 2019 anomalies are consistent with the negative Southern Oscillation index (SOI), a measure of the surface pressure difference between Tahiti and Darwin, for August–September 2019, indicating El Niño conditions (NCEI 2025b). The Oceanic Niño index (ONI), representing SST anomalies in the Niño-3.4 region (120°–170°W), indicates more neutral conditions for August–September 2019 (NCEI 2025a), suggesting weak El Niño forcing. In contrast, during 2022, the SOI and ONI both indicate La Niña conditions for August–September, again consistent with the SST and 850-hPa wind anomalies present in 2022.

SST warm anomalies in the east Pacific have been found to play a role in favoring increased TEW track density and strength (Serra and Geil 2017). Studies also suggest TEW tracks shift south during El Niño years when the Western Hemisphere warm pool is stronger and extended more southward than normal (Bengtsson et al. 2006; Dominguez et al. 2020), which may bring more waves over Costa Rica. That being said, the similar number of TEWs during 2019 and 2022 based on the TD OLR at LIMO suggests that ENSO had a minimal impact on OTREC TEW track density. In addition, we find no discernible difference in the median TD OLR negative anomaly at LIMO in 2019 or 2022 when compared to climatology (not shown), suggesting minimal impact of ENSO on OTREC TEW wave strength.

ENSO also has impacts on precipitation patterns over Costa Rica (Waylen et al. 1996), with enhanced rainfall on the Caribbean coast and dry conditions on the Pacific coast observed during boreal summer for El Niño years, with opposite anomalies during La Niña years. Consistent with this climatology, in August 2019, the Centro Internacional Para la Investigación del Fenómeno El Niño (CIIFEN) reports anomalously dry conditions on the Guanacaste Peninsula and west coast of Costa Rica, while the east coast near Limón was

anomalously wet (CIIFEN 2025a). In contrast, in August 2022, CIIFEN reports wet conditions on the Guanacaste Peninsula and dry conditions on the east coast of Costa Rica (CIIFEN 2025b). While we composite these two opposing ENSO years for this study for five of our sites, without a neutral year for comparison, it is difficult to know the extent to which ENSO impacts our results.

The Madden–Julian oscillation (MJO) is a dominant mode of intraseasonal variability in the tropics and has been found to modulate TEWs and hurricane activity in the Caribbean and eastern Pacific region (e.g., Maloney and Hartmann 2000; Crosbie and Serra 2014; Rydbeck and Maloney 2014; Whitaker and Maloney 2018). The real-time multivariate MJO (RMM) index (Wheeler and Hendon 2004; Gottschalck et al. 2010), a measure of the global MJO activity, exceeded an amplitude of one after 14 September 2019 in the Western Hemisphere quadrant (see Fig. S2a). Figure 3a shows several TEWs crossing the southern portion of Central America within 5°–10°N from 24 August to 19 September, followed by an absence of waves after this date. This is consistent with the northward shift in TEW tracks across Central America during the active MJO phase evident in the low-level vorticity anomaly composites of Whitaker and Maloney (2018). Active (westerly) MJO events, like El Niño events, result in dry conditions on the east coast of Costa Rica and wet conditions on the west coast, with the opposite situation during MJO suppressed (easterly) phases (Crosbie and Serra 2014; Whitaker and Maloney 2018). This appears to mainly be the result of moisture convergence anomalies along the coastlines of Central America related to MJO low-level zonal wind anomalies (Crosbie and Serra 2014). Further investigation of in situ datasets, while outside the scope of this study, is needed to better understand the full impact of the MJO on Central American meteorological variables including rainfall in 2019.

The RMM index for 2022 indicates that the MJO was active from 21–26 July to 21–30 August (Fig. S2b). As our radiosonde launches were from 29 July to 12 August, we do not expect any influence of the MJO on our 2022 sounding analyses and minimal influence on the surface network analyses given the short duration of the August event.

6. Summary and conclusions

TEWs are widely recognized as one of the principal phenomena mediating regional weather variability over many tropical land areas, including Central America. However, existing mechanistic understanding of the connection between rainfall and TEWs over Central America has been limited, in large part due to the lack of comprehensive measurements. Leveraging observations from the 2019 OTREC field campaign, along with additional measurements in 2022, we have presented in this study analyses that inform how TEWs affect rainfall over land. In particular, we have focused on elucidating the interplay of the synoptic-scale dynamics and thermodynamics over the life cycle of TEWs with the diurnal cycle of rainfall over Costa Rica.

From our analysis of both the soundings and OTREC surface meteorology, we have demonstrated signatures of TEW propagation and how these evolve across Costa Rica. The vertical structure of temperature, moisture, and wind anomalies during TEW passages suggests that for the waves captured by this dataset, favorable temperature anomalies are observed coupled to convection along the Caribbean coast of Costa Rica for active TEW phases, while less favorable temperature profiles are observed at our site on the Guanacaste Peninsula north and east of the main east–west transect captured by our surface network. This suggests that core convection associated with these TEWs develops south of Guanacaste, consistent with typical TEW vorticity tracks across Costa Rica (e.g., Kerns et al. 2008; Serra et al. 2010). In addition, ERA5 vertical velocity anomalies suggest more shallow development of convection along the Caribbean coast, while inland regions show more extensive stratiform and deep convective regions. For cases in which the active phase of a TEW is associated with the development of severe weather conditions, the identification of differences in the convection cores' location can contribute to providing a better characterization of precipitation extreme impact hotspots. Furthermore, analyzing this characteristic provides a foundation upon which the influence of low-frequency modes of variability such as ENSO alters the precipitation distribution and intensity across Costa Rica and in particular at hotspots of extreme precipitation in the region.

Rainfall, PWV, and CTT also manifest a general east-to-west progression that can be understood in terms of "envelopes" of convectively favorable or unfavorable synoptic conditions that comprise the active and suppressed phases of a TEW. However, the signatures of propagation in rainfall, PWV, and CTT are more pronounced for the active phase conditions compared to the suppressed phase, which we speculate may be the result of how TEWs couple with the diurnal cycle, as discussed further below. The time scale for such propagation from the Caribbean to the Pacific coasts is approximately 12 h, which translates to a propagation speed of ~6.5 m s^{-1}. This locally based estimate of phase speed is on the low side of values reported previously for TEWs over the Caribbean and east Pacific (e.g., 5.0–12.7 m s^{-1}: Kerns et al. 2008; 11.3–13.6 m s^{-1}: Serra et al. 2008), although it is unclear whether it represents a systematic difference in wave propagation over the region or limitations of the dataset (e.g., the small number of waves observed, seasonal sampling effects). These results are consistent with African easterly waves, for which slower phase speeds are reported over land than offshore in the eastern Atlantic (e.g., Carlson 1969). Accurate estimation tools for estimating TEW propagation speed are useful for operational forecasts, which otherwise use objective methods to generate this information to inform forecasters.

We have also assessed the connection between the diurnal cycle of rainfall and TEWs. For the Caribbean coastal region of Costa Rica (CARIB), TEW active phases are associated with a morning maximum in rainfall, in contrast to neutral and suppressed phases, which exhibit afternoon maxima. Broadly, over the tropics, ocean regions are associated with diurnal cycles peaking in the early morning, while land regions are associated with afternoon or evening diurnal maxima; thus, qualitatively, the diurnal behavior evident at the Caribbean coastal sites implicates a transition from a more

oceanic regime during TEW active phases to the more terrestrial regime during neutral and suppressed TEW phases. Inland and Pacific sites, on the other hand, show diurnal cycles with characteristic afternoon to evening maxima; however, under the influence of TEW active phases, the onset of convection and increase in PWV occur somewhat earlier for inland sites. For the Caribbean and inland locations, the duration of rain events is greater during the active phase, while no clear increase in the magnitude of events is apparent for any region. This result is very relevant as it provides evidence of an oceanic-to-terrestrial regime transition for Costa Rica rather than the fully oceanic regime commonly assumed. OTREC observations suggest that models used for the region must include better surface parameterization and potentially integrate coupling with land surface models. The apparent role of the surface in the shaping of precipitation characteristics in the OTREC data also draws attention to the potential sensitivity of precipitation to changes in the land surface (e.g., deforestation, land use, and vegetation coverage changes).

The interplay of TEWs with local-scale circulations such as sea breezes and how this interplay may shape the way TEWs modulate diurnal rainfall was also examined. Indeed, sea breezes appear to contribute to the diurnal cycle in rainfall along both coasts of Costa Rica, with peak rainfall following peak late morning onshore flow at these sites. This peak onshore flow precedes peak PWV at all sites and for the active, suppressed, and neutral composites. The exception is the active period along the Caribbean coast, during which early morning convection reduces daytime heating and likely contributes to the suppressed sea-breeze circulations at this time. In addition, PWV peaks early in the morning along the Caribbean coast with the arrival of the TEW for the active phase and is thus not in sync with the sea-breeze circulations for these periods.

Our analysis does raise some questions that we are unable to resolve with the existing data. One question involves the extent to which the timing of TEW arrival affects the diurnal cycle, for example, does a TEW arriving at noon have the same impact as one arriving at midnight? Is the observed progression of TEW convective activity indicative of an optimal phasing of TEW convection and the diurnal cycle at our inland sites? In our analysis, we have not attempted stratification of TEWs by arrival, in part because of the limited amount of OTREC data and because the TD index only enables assessment of wave phase on half-day time scales. Of course, given that the conditions associated with a particular phase extend over synoptic scales, identifying wave arrival may not be straightforward.

Acknowledgments. We would like to acknowledge the important contributions of the Instituto Meteorológico Nacional de Costa Rica, David Adams of Universidad Nacional Autónoma de México, David Gochis of the National Center for Atmospheric Research's Research Applications Laboratory; Jim Normandeau of UNAVCO; Marino Protti, Germain Esquivel and Ricardo Sánchez of the Universidad Nacional de Costa Rica; Tim Melbourne of Central Washington University; Evelyn Quirós and personnel from Aviación Civil that provided operation space at Limón Airport and coordination for the launches; Tiffany Suárez from the transportation unit, Sede de Santa Cruz, CIGEFI, EEAFBM; the Director of Research at Universidad de Costa Rica for operational support; and all OTREC field campaign participants who helped install and maintain the Surface GPS-Met Network for OTREC: Armando Aguilar, Rodrigo Castillo, Maureen Fonseca, Marcial Garbanzo, Lidia Huaman, Paulo Solano, Beata Latos, Fernando Lezana, Ruben Madrigal, Gabriel Maynard, Lourdes Mendoza, María Mercedes, Natalia Mora, Raquel Ramírez, Yakelyn Ramos, Alberto Salazar, Sarah Tannenbaum, Rani Wiggins, Kuang Zheng, José Miguel Araya, and Cristian Porras. Finally, we thank the landowners who kindly opened their houses and provided space, electricity, and internet connections for the surface network. This work would not have been possible without the dedication of these scientists, engineers, students, and citizens. This work was supported by the U.S. National Science Foundation Grant AGS-1758666. This publication is partially funded by the Cooperative Institute for Climate, Ocean, and Ecosystem Studies (CICOES) under NOAA Cooperative Agreement NA20OAR4320271, Contribution 2025-1455.

Data availability statement. The GPS-Met and radiosonde data from OTREC 2019 are available from the Earth Observing Laboratory (EOL) OTREC data server (GPS-Met: https://doi.org/10.26023/ATW3-HC63-ED00, STCZ: https://doi.org/10.26023/1YXF-N0Q1-VJ0C, LIMO: https://doi.org/10.26023/9KHX-9BBH-TX0E). Hourly surface meteorological data at LIMO, TURR, CGFI, and STCZ for 2022 are available from the Costa Rican Meteorological Service (https://www.imn.ac.cr/web/imn/solicitud-de-servicios). COCONet 1-min GPS receiver data at VRAI for 2022 are available from UNAVCO (https://www.unavco.org/data/doi/10.7283/T5RX99C1). The additional radiosonde data collected during 2022 at STCZ and LIMO, as well as the 2022 1-min PWV calculated at VRAI, are available upon request from Dr. Yolande Serra (yserra@uw.edu). Twice-daily outgoing longwave radiation data can be requested from the NOAA Physical Sciences Laboratory (psl.data@noaa.gov).

REFERENCES

Adams, D. K., and Coauthors, 2011: A dense GNSS meteorological network for observing deep convection in the Amazon. *Atmos. Sci. Lett.*, **12**, 207–212, https://doi.org/10.1002/asl.312.

——, S. I. Gutman, K. L. Holub, and D. S. Pereira, 2013: GNSS observations of deep convective time scales in the Amazon. *Geophys. Res. Lett.*, **40**, 2818–2823, https://doi.org/10.1002/grl.50573.

——, and Coauthors, 2015: The Amazon dense GNSS meteorological network: A new approach for examining water vapor and deep convection interactions in the tropics. *Bull. Amer. Meteor. Soc.*, **96**, 2151–2165, https://doi.org/10.1175/BAMS-D-13-00171.1.

Amador, J. A., and E. J. Alfaro, 2014: Weather and climate socio-economic impacts in Central America for the management and protection of world heritage sites and the Diquis Delta culture in Costa Rica (a case study). *Adv. Geosci.*, **35**, 157–167, https://doi.org/10.5194/adgeo-35-157-2014.

Avila, L. A., and R. J. Pasch, 1995: Atlantic tropical systems of 1993. *Mon. Wea. Rev.*, **123**, 887–896, https://doi.org/10.1175/1520-0493(1995)123<0887:ATSO>2.0.CO;2.

Bengtsson, L., K. I. Hodges, and E. Roeckner, 2006: Storm tracks and climate change. *J. Climate*, **19**, 3518–3543, https://doi.org/10.1175/JCLI3815.1.

Burpee, R. W., 1972: The origin and structure of easterly waves in the lower troposphere of North Africa. *J. Atmos. Sci.*, **29**, 77–90, https://doi.org/10.1175/1520-0469(1972)029<0077:TOASOE>2.0.CO;2.

Carlson, T. N., 1969: Some remarks on African disturbances and their progress over the tropical Atlantic. *Mon. Wea. Rev.*, **97**, 716–726, https://doi.org/10.1175/1520-0493(1969)097<0716:SROADA>2.3.CO;2.

Cheng, Y.-M., J. Dias, G. Kiladis, Z. Feng, and L. R. Leung, 2023: Mesoscale convective systems modulated by convectively coupled equatorial waves. *Geophys. Res. Lett.*, **50**, e2023GL103335, https://doi.org/10.1029/2023GL103335.

CIIFEN, 2025a: El Niño/La Niña in Latin America September 2019. 21 pp., https://ciifen.org/wp-content/uploads/2020/09/9-SEPTIEMBRE-2019-EL-NINO.pdf.

——, 2025b: El Niño/La Niña in Latin America August 2022. 28 pp., https://ciifen.org/wp-content/uploads/2022/08/Boletin_CIIFEN_agosto_2022.pdf.

Crosbie, E., and Y. Serra, 2014: Intraseasonal modulation of synoptic-scale disturbances and tropical cyclone genesis in the eastern North Pacific. *J. Climate*, **27**, 5724–5745, https://doi.org/10.1175/JCLI-D-13-00399.1.

Dominguez, C., J. M. Done, and C. L. Bruyère, 2020: Easterly wave contributions to seasonal rainfall over the tropical Americas in observations and a regional climate model. *Climate Dyn.*, **54**, 191–209, https://doi.org/10.1007/s00382-019-04996-7.

Fuchs-Stone, Ž., D. J. Raymond, and S. Sentić, 2020: OTREC2019: Convection over the East Pacific and southwest Caribbean. *Geophys. Res. Lett.*, **47**, e2020GL087564, https://doi.org/10.1029/2020GL087564.

Gottschalck, J., and Coauthors, 2010: A framework for assessing operational Madden–Julian oscillation forecasts. *Bull. Amer. Meteor. Soc.*, **91**, 1247–1258, https://doi.org/10.1175/2010BAMS2816.1.

Hersbach, H., and Coauthors, 2020: The ERA5 global reanalysis. *Quart. J. Roy. Meteor. Soc.*, **146**, 1999–2049, https://doi.org/10.1002/qj.3803.

Hersbach, H, and Coauthors, 2023: ERA5 hourly data on pressure levels from 1940 to present. Copernicus Climate Change Service (C3S) Climate Data Store (CDS), accessed on 9 May 2023, https://doi.org/10.24381/cds.bd0915c6.

Hollis, M. A., R. R. McCrary, J. P. Stachnik, C. Lewis-Merritt, and E. R. Martin, 2024: A global climatology of tropical easterly waves. *Climate Dyn.*, **62**, 2317–2332, https://doi.org/10.1007/s00382-023-07025-w.

Holloway, C. E., and J. D. Neelin, 2010: Temporal relations of column water vapor and tropical precipitation. *J. Atmos. Sci.*, **67**, 1091–1105, https://doi.org/10.1175/2009JAS3284.1.

Huaman, L., E. D. Maloney, C. Schumacher, and G. N. Kiladis, 2021: Easterly waves in the East Pacific during the OTREC 2019 field campaign. *J. Atmos. Sci.*, **78**, 4071–4088, https://doi.org/10.1175/JAS-D-21-0128.1.

Kerns, B., K. Greene, and E. Zipser, 2008: Four years of tropical ERA-40 vorticity maxima tracks. Part I: Climatology and vertical vorticity structure. *Mon. Wea. Rev.*, **136**, 4301–4319, https://doi.org/10.1175/2008MWR2390.1.

Kiladis, G. N., M. C. Wheeler, P. T. Haertel, K. H. Straub, and P. E. Roundy, 2009: Convectively coupled equatorial waves. *Rev. Geophys.*, **47**, RG2003, https://doi.org/10.1029/2008RG000266.

Landsea, C. W., 1993: A climatology of intense (or major) Atlantic hurricanes. *Mon. Wea. Rev.*, **121**, 1703–1713, https://doi.org/10.1175/1520-0493(1993)121<1703:ACOIMA>2.0.CO;2.

Liebmann, B., and C. A. Smith, 1996: Description of a complete (interpolated) outgoing longwave radiation dataset. *Bull. Amer. Meteor. Soc.*, **77**, 1275–1277.

Liu, C., and E. J. Zipser, 2008: Diurnal cycles of precipitation, clouds, and lightning in the tropics from 9 years of TRMM observations. *Geophys. Res. Lett.*, **35**, L04819, https://doi.org/10.1029/2007GL032437.

Maldonado, T., E. Alfaro, B. Fallas-López, and L. Alvarado, 2013: Seasonal prediction of extreme precipitation events and frequency of rainy days over Costa Rica, Central America, using canonical correlation analysis. *Adv. Geosci.*, **33**, 41–52, https://doi.org/10.5194/adgeo-33-41-2013.

Maloney, E. D., and D. L. Hartmann, 2000: Modulation of hurricane activity in the Gulf of Mexico by the Madden-Julian oscillation. *Science*, **287**, 2002–2004, https://doi.org/10.1126/science.287.5460.2002.

Mapes, B. E., and R. A. Houze Jr., 1995: Diabatic divergence profiles in western Pacific mesoscale convective systems. *J. Atmos. Sci.*, **52**, 1807–1828, https://doi.org/10.1175/1520-0469(1995)052<1807:DDPIWP>2.0.CO;2.

Mejía, J. F., J. Yepes, J. J. Henao, G. Poveda, M. D. Zuluaga, D. J. Raymond, and Ž. Fuchs-Stone, 2021: Towards a mechanistic understanding of precipitation over the Far Eastern tropical Pacific and western Colombia, one of the rainiest spots on Earth. *J. Geophys. Res. Atmos.*, **126**, e2020JD033415, https://doi.org/10.1029/2020jd033415.

Méndez, M., and V. Magaña, 2010: Regional aspects of prolonged meteorological droughts over Mexico and Central America. *J. Climate*, **23**, 1175–1188, https://doi.org/10.1175/2009JCLI3080.1.

Molinari, J., D. Knight, M. Dickinson, D. Vollaro, and S. Skubis, 1997: Potential vorticity, easterly waves, and eastern Pacific tropical cyclogenesis. *Mon. Wea. Rev.*, **125**, 2699–2708, https://doi.org/10.1175/1520-0493(1997)125<2699:PVEWAE>2.0.CO;2.

Mora, N., J. A. Amador, E. R. Rivera, and T. Maldonado, 2020: A sea breeze study during ticosonde-NAME 2004 in the Central Pacific of Costa Rica: Observations and numerical modeling. *Atmosphere*, **11**, 1333, https://doi.org/10.3390/atmos11121333.

Muñoz, E., A. J. Busalacchi, S. Nigam, and A. Ruiz-Barradas, 2008: Winter and summer structure of the Caribbean low-level jet. *J Climate*, **21**, 1260–1276, https://doi.org/10.1175/2007JCLI1855.1.

NCEI, 2025a: Ocean Niño Index. Accessed 5 June 2025, https://www.cpc.ncep.noaa.gov/data/indices/oni.ascii.txt.

——, 2025b: Southern Oscillation Index. Accessed 5 June 2025, https://www.cpc.ncep.noaa.gov/data/indices/soi.

Nesbitt, S. W., and E. J. Zipser, 2003: The diurnal cycle of rainfall and convective intensity according to three years of TRMM

measurements. *J. Climate*, **16**, 1456–1475, https://doi.org/10.1175/1520-0442-16.10.1456.

NHC, 2025: Unified Surface Analysis Archive. Accessed 12 May 2025, https://ftp.nhc.ncep.noaa.gov/tafb/surface_analysis/2019/08/.

Nitta, T., and Y. Takayabu, 1985: Global analysis of the lower tropospheric disturbances in the tropics during the Northern summer of the FGGE year part II: Regional characteristics of the disturbances. *Pure Appl. Geophys.*, **123**, 272–292, https://doi.org/10.1007/BF00877023.

Norquist, D. C., E. E. Recker, and R. J. Reed, 1977: The energetics of African wave disturbances as observed during phase III of GATE. *Mon. Wea. Rev.*, **105**, 334–342, https://doi.org/10.1175/1520-0493(1977)105<0334:TEOAWD>2.0.CO;2.

Peatman, S. C., A. J. Matthews, and D. P. Stevens, 2014: Propagation of the Madden–Julian Oscillation through the Maritime Continent and scale interaction with the diurnal cycle of precipitation. *Quart. J. Roy. Meteor. Soc.*, **140**, 814–825, https://doi.org/10.1002/qj.2161.

Petersen, W. A., R. Cifelli, D. J. Boccippio, S. A. Rutledge, and C. Fairall, 2003: Convection and easterly wave structures observed in the eastern Pacific warm pool during EPIC-2001. *J. Atmos. Sci.*, **60**, 1754–1773, https://doi.org/10.1175/1520-0469(2003)060<1754:CAEWSO>2.0.CO;2.

Raymond, D. J., and Coauthors, 2004: EPIC2001 and the coupled ocean–atmosphere system of the tropical East Pacific. *Bull. Amer. Meteor. Soc.*, **85**, 1341–1354, https://doi.org/10.1175/BAMS-85-9-1341.

Reed, R. J., D. C. Norquist, and E. E. Recker, 1977: The structure and properties of African wave disturbances as observed during phase III of GATE. *Mon. Wea. Rev.*, **105**, 317–333, https://doi.org/10.1175/1520-0493(1977)105<0317:TSAPOA>2.0.CO;2.

Roundy, P. E., and W. M. Frank, 2004: A climatology of waves in the equatorial region. *J. Atmos. Sci.*, **61**, 2105–2132, https://doi.org/10.1175/1520-0469(2004)061<2105:ACOWIT>2.0.CO;2.

Ruppert, J. H., Jr., and R. H. Johnson, 2015: Diurnally modulated cumulus moistening in the preonset stage of the Madden–Julian oscillation during DYNAMO. *J. Atmos. Sci.*, **72**, 1622–1647, https://doi.org/10.1175/JAS-D-14-0218.1.

Rydbeck, A. V., and E. D. Maloney, 2014: Energetics of East Pacific easterly waves during intraseasonal events. *J Climate*, **27**, 7603–7621, https://doi.org/10.1175/JCLI-D-14-00211.1.

——, and ——, 2015: On the convective coupling and moisture organization of East Pacific easterly waves. *J. Atmos. Sci.*, **72**, 3850–3870, https://doi.org/10.1175/JAS-D-15-0056.1.

Schumacher, C., R. A. Houze, Jr., and I. Kraucunas, 2004: The tropical dynamical response to latent heating estimates derived from the TRMM precipitation radar. *J. Atmos. Sci.*, **61**, 1341–1358, https://doi.org/10.1175/1520-0469(2004)061<1341:TTDRTL>2.0.CO;2.

Sentić, S., 2020: Upper-air measurements at Santa Cruz, Costa Rica. Version 1.0. UCAR/NCAR—Earth Observing Laboratory, accessed 4 October 2023, https://doi.org/10.26023/1YXF-N0Q1-VJ0C.

Serra, Y. L., and R. A. Houze, Jr., 2002: Observations of variability on synoptic timescales in the East Pacific ITCZ. *J. Atmos. Sci.*, **59**, 1723–1743, https://doi.org/10.1175/1520-0469(2002)059<1723:OOVOST>2.0.CO;2.

——, and K. Geil, 2017: Historical and projected eastern Pacific and intra-Americas sea TD-wave activity in a selection of IPCC AR5 models. *J. Climate*, **30**, 2269–2294, https://doi.org/10.1175/JCLI-D-16-0453.1.

——, G. N. Kiladis, and M. F. Cronin, 2008: Horizontal and vertical structure of easterly waves in the Pacific ITCZ. *J. Atmos. Sci.*, **65**, 1266–1284, https://doi.org/10.1175/2007JAS2341.1.

——, ——, and K. I. Hodges, 2010: Tracking and mean structure of easterly waves over the intra-Americas sea. *J Climate*, **23**, 4823–4840, https://doi.org/10.1175/2010JCLI3223.1.

——, and Coauthors, 2020a: OTREC surface GPS-Met network. Version 1.0. UCAR/NCAR—Earth Observing Laboratory, accessed 4 October 2023, https://doi.org/10.26023/ATW3-HC63-ED00.

——, and Coauthors, 2020b: Radiosonde data from Limon, Costa Rica. Version 1.1. UCAR/NCAR—Earth Observing Laboratory, accessed 4 October 2023, https://doi.org/10.26023/9KHX-9BBH-TX0E.

——, A. Rowe, D. K. Adams, and G. N. Kiladis, 2020c: Kelvin waves during GOAmazon and their relationship to deep convection. *J. Atmos. Sci.*, **77**, 3533–3550, https://doi.org/10.1175/JAS-D-20-0008.1.

Sobel, A. H., C. D. Burleyson, and S. E. Yuter, 2011: Rain on small tropical islands. *J. Geophys. Res.*, **116**, D08102, https://doi.org/10.1029/2010JD014695.

Straub, K. H., and G. N. Kiladis, 2002: Observations of a convectively coupled kelvin wave in the eastern Pacific ITCZ. *J. Atmos. Sci.*, **59**, 30–53, https://doi.org/10.1175/1520-0469(2002)059<0030:OOACCK>2.0.CO;2.

Thorncroft, C. D., and B. J. Hoskins, 1994: An idealized study of African easterly waves. I: A linear view. *Quart. J. Roy. Meteor. Soc.*, **120**, 953–982, https://doi.org/10.1002/qj.49712051809.

——, N. M. J. Hall, and G. N. Kiladis, 2008: Three-dimensional structure and dynamics of African easterly waves. Part III: Genesis. *J. Atmos. Sci.*, **65**, 3596–3607, https://doi.org/10.1175/2008JAS2575.1.

Torres, V. M., C. D. Thorncroft, and N. M. J. Hall, 2021: Genesis of easterly waves over the tropical eastern Pacific and the intra-Americas sea. *J. Atmos. Sci.*, **78**, 3263–3279, https://doi.org/10.1175/JAS-D-20-0389.1.

Torri, G., D. K. Adams, H. Wang, and Z. Kuang, 2019: On the diurnal cycle of GPS-derived precipitable water vapor over Sumatra. *J. Atmos. Sci.*, **76**, 3529–3552, https://doi.org/10.1175/JAS-D-19-0094.1.

Ulrich, M., and G. Bellon, 2019: Superenhancement of precipitation at the center of tropical islands. *Geophys. Res. Lett.*, **46**, 14 872–14 880, https://doi.org/10.1029/2019GL084947.

Wang, C., 2007: Variability of the Caribbean low-level jet and its relations to climate. *Climate Dyn.*, **29**, 411–422, https://doi.org/10.1007/s00382-007-0243-z.

Waylen, P. R., C. N. Caviedes, and M. E. Quesada, 1996: Interannual variability of monthly precipitation in Costa Rica. *J. Climate*, **9**, 2606–2613, https://doi.org/10.1175/1520-0442(1996)009<2606:IVOMPI>2.0.CO;2.

Wheeler, M., and G. N. Kiladis, 1999: Convectively coupled equatorial waves: Analysis of clouds and temperature in the wavenumber-frequency domain. *J. Atmos. Sci.*, **56**, 374–399, https://doi.org/10.1175/1520-0469(1999)056<0374:ccewao>2.0.co;2.

Wheeler, M. C., and H. H. Hendon, 2004: An all-season real-time multivariate MJO index: Development of an index for monitoring and prediction. *Mon. Wea. Rev.*, **132**, 1917–1932, https://doi.org/10.1175/1520-0493(2004)132<1917:AARMMI>2.0.CO;2.

Whitaker, J. W., and E. D. Maloney, 2018: Influence of the Madden–Julian oscillation and Caribbean low-level jet on East Pacific easterly wave dynamics. *J. Atmos. Sci.*, **75**, 1121–1141, https://doi.org/10.1175/JAS-D-17-0250.1.

Wiggins, R. M., B. R. Lintner, Y. L. Serra, A. M. Durán-Quesada, M. Garbanzo-Salas, D. Hernández-Deckers, and G. Torri, 2023: Tropical easterly waves over Costa Rica and their relationship to the diurnal cycle of rainfall. *Geophys. Res. Lett.*, **50**, e2023GL104159, https://doi.org/10.1029/2023GL104159.

Yang, G.-Y., and J. Slingo, 2001: The diurnal cycle in the tropics. *Mon. Wea. Rev.*, **129**, 784–801, https://doi.org/10.1175/1520-0493(2001)129<0784:TDCITT>2.0.CO;2.

Yasunaga, K., and B. Mapes, 2012a: Differences between more divergent and more rotational types of convectively coupled equatorial waves. Part I: Space–time spectral analyses. *J. Atmos. Sci.*, **69**, 3–16, https://doi.org/10.1175/JAS-D-11-033.1.

——, and ——, 2012b: Differences between more divergent and more rotational types of convectively coupled equatorial waves. Part II: Composite analysis based on space–time filtering. *J. Atmos. Sci.*, **69**, 17–34, https://doi.org/10.1175/JAS-D-11-034.1.